9-7-2019

WALLABY early science – V. ASKAP HI imaging of the Lyon Group of Galaxies 351

B. Q. For
University of Western Australia

L. Staveley-Smith
University of Western Australia

T. Westmeier
University of Western Australia

M. Whiting
CSIRO Astronomy and Space Science

S. -H. Oh
Sejong University

Authors

B. Q. For, L. Staveley-Smith, T. Westmeier, M. Whiting, S. -H. Oh, B. Koribalski, J. Wang, O. I. Wong, G. Bekiaris, L. Cortese, A. Elagali, D. Kleiner, K. Lee-Waddell, Juan P. Madrid, A. Popping, J. Rhee, T. N. Reynolds, J. D. Collier, C. J. Phillips, M. A. Voronkov, O. Mueller, and H. Jerjen

WALLABY early science − V. ASKAP H I imaging of the Lyon Group of Galaxies 351

B.-Q. For [1,2]★ L. Staveley-Smith [1,2] T. Westmeier [1,2] M. Whiting,[3] S.-H. Oh,[4]
B. Koribalski [3,2] J. Wang,[5] O. I. Wong,[1,2] G. Bekiaris,[3] L. Cortese [1,2] A. Elagali,[1,2,3]
D. Kleiner [3,6] K. Lee-Waddell [3,2] J. P. Madrid,[3,7] A. Popping,[1] J. Rhee [1,2]
T. N. Reynolds [1,2,3] J. D. Collier,[3,8,9] C. J. Phillips,[3] M. A. Voronkov,[3] O. Müller[10]
and H. Jerjen[11]

[1]*International Centre for Radio Astronomy Research, University of Western Australia, 35 Stirling Hwy, Crawley, WA 6009, Australia*
[2]*ARC Centre of Excellence for All Sky Astrophysics in 3 Dimensions (ASTRO 3D)*
[3]*CSIRO Astronomy and Space Science (CASS), PO Box 76, Epping, NSW 1710, Australia*
[4]*Department of Physics and Astronomy, Sejong University, 209 Neungdong-ro, Gwangjin-gu, Seoul 05006, Republic of Korea*
[5]*Kavli Institute for Astronomy and Astrophysics, Peking University, Beijing 100871, China*
[6]*INAF Osservatorio Astronomico di Cagliari, Via della Scienza 5, I-09047 Selargius (CA), Italy*
[7]*Department of Physics and Astronomy, University of Texas Rio Grande Valley, One West University Blvd, Brownsville, TX 78520, USA*
[8]*School of Computing, Engineering and Mathematics, Western Sydney University, Locked Bag 1797, Penrith, NSW 2751, Australia*
[9]*Department of Astronomy, The Inter-University Institute for Data Intensive Astronomy (IDIA), University of Cape Town, Rondebosch 7701, South Africa*
[10]*CNRS, Observatoire astronomique de Strasbourg (ObAS), Université de Strasbourg, UMR 7550, F-67000 Strasbourg, France*
[11]*Research School of Astronomy and Astrophysics, Australian National University, Canberra, ACT 2611, Australia*

ABSTRACT

We present an H I study of the galaxy group LGG 351 using Widefield ASKAP *L*-band Legacy All-sky Blind Survey (WALLABY) early science data observed with the Australian Square Kilometre Array Pathfinder (ASKAP). LGG 351 resides behind the M 83 group at a velocity range (*cz*) of ∼3500–4800 km s^{-1} within the rich Hydra-Centaurus overdensity region. We detect 40 sources with the discovery of a tidally interacting galaxy pair and two new H I sources that are not presented in previous optical catalogues. 23 out of 40 sources have new redshifts derived from the new H I data. This study is the largest WALLABY sub-sample to date and also allows us to further validate the performance of ASKAP and the data reduction pipeline ASKAPSOFT. Extended H I emission is seen in six galaxies indicating interaction within the group, although no H I debris is found. We also detect H I in a known ultra-faint dwarf galaxy (dw 1328−29), which demonstrates that it is not a satellite of the M 83 group as previously thought. In conjunction with multiwavelength data, we find that our galaxies follow the atomic gas fraction and baryonic Tully–Fisher scaling relations derived from the GALEX Arecibo SDSS Survey. In addition, majority of our galaxies fall within the star formation main sequence indicating inefficiency of gas removal processes in this loose galaxy group.

Key words: instrumentation: interferometer – galaxies: distances and redshifts – galaxies: groups: general – galaxies: interactions – galaxies: star formation.

1 INTRODUCTION

The environment in which galaxies are residing and evolving is thought to affect their fundamental properties, such as the morphology, colour, and star formation rate. Observations show that the fraction of late-type (spiral and irregular) galaxies in clusters increases with increasing redshift (Butcher & Oemler 1978; Oh et al. 2018a). Dressler (1980) highlighted the existence of a morphology–density relation, in which the fraction of early-type galaxies increases while the fraction of late-type galaxies decreases with increasing galaxy density. Studies have also revealed suppression of star formation in dense environments (e.g. Lewis et al. 2002; Kauffmann et al. 2004; Cortese et al. 2019). This evidence clearly shows that environmental effects play a significant role in galaxy evolution.

★ E-mail: biqing.for@uwa.edu.au

As gas serves as a reservoir to fuel star formation, it is crucial to investigate the effectiveness of gas removal and accretion processes in environments of different density. To sustain ongoing star formation, a constant replenishment of gas is vital or else the galaxies would quench and become red and passive (Larson, Tinsley & Caldwell 1980). For gas accretion processes, cosmological models with cold and hot mode accretion have been postulated through numerical hydrodynamical simulations (Katz et al. 2003; Kereš et al. 2005). In the cold mode, fresh gas tunnels via filaments and accretes directly into the low- to intermediate-mass halo of galaxies. Hot mode accretion involves gas being shock-heated to high temperatures at the virial radius, and later cooling and falling into the galaxy centre. As a result, accretion processes via the cold mode are expected to dominate high-redshift ($z \geq 1$) galaxies, while the hot mode is expected to dominate high-density and high-mass ($M_* > 10^{10.5}$ $M_\odot$) low-redshift ($z < 1$) galaxies (Dekel & Birnboim 2006; van de Voort et al. 2011).

The gas removal processes can occur through two main mechanisms: (i) ram-pressure stripping, when a galaxy passes through a dense intergalactic medium (IGM) and (ii) tidal stripping due to gravitational interaction. The first mechanism is well observed in high-density clusters (see e.g. Chung et al. 2009; Vollmer et al. 2012) but it has also been observed in low-density galaxy groups (Westmeier, Braun & Koribalski 2011; Rasmussen et al. 2012; Catinella et al. 2013; Brown et al. 2017). The second mechanism is more commonly observed in small groups, where relative velocities between galaxies are low (see e.g. Koribalski & López-Sánchez 2009; For, Staveley-Smith & McClure-Griffiths 2013; For et al. 2014). These mechanisms can result in a galaxy losing its hot halo and quenching of the star formation process. Quenching can occur in both cluster and group environments. Neutral hydrogen (H I) gas is a good tracer for studying these mechanisms in star-forming and H I rich galaxies as it is generally more extended than the stellar disc and is much more sensitive to any disturbance by the environment (Hibbard & van Gorkom 1996).

There have been studies of H I content and physical processes that affect galaxies in a wide range of environments, from voids to clusters and groups. Most notable studies are through single-dish H I surveys like the Northern hemisphere Arecibo Legacy Fast ALFA survey (ALFALFA; Giovanelli et al. 2005) and the H I Parkes All-Sky Survey (HIPASS; Barnes et al. 2001). The angular resolution of these surveys is limited to arcminutes which is usually insufficient to resolve gas discs and H I debris. Interferometers offer higher angular resolution but often at the cost of sensitivity to low column densities, and therefore require more observing time to reach the equivalent sensitivity of a single-dish telescope. Thus, they have been limited to small-scale target-specific surveys and resulted in biased samples for environmental studies. With new widefield H I surveys at sub-arcminute angular resolution commencing using radio telescopes such as the Australian Square Kilometre Array Pathfinder (ASKAP; Johnston et al. 2007), it will become possible to build an unbiased statistical sample of galaxies for investigating environmental effects.

The Widefield ASKAP *L*-Band Legacy All-sky Blind surveY (WALLABY) is one of the key ASKAP science projects. The survey is designed to cover 3π steradian of sky ($-90° < \delta < +30°$) with an angular resolution of 30 arcsec and a spectral resolution of 4 km s^{-1} at $z = 0$. It is expected to detect the H I emission of more than 500 000 galaxies out to a redshift of 0.26 (Duffy et al. 2012). The detection rate will be an order of magnitude higher than that of the HIPASS and ALFALFA surveys. The estimated root-mean-square (RMS) noise level is 1.7 mJy per beam per 4 km s^{-1} (Koribalski et al., in preparation).

1.1 The Lyon Group of Galaxies 351

In this section, we provide some background information on the LGG 351 group, also known as NGC 5135 galaxy group. NGC 5135 has previously selected as part of the environmental study of galaxy groups that consist of Seyfert galaxies (Kollatschny & Fricke 1989, hereafter KF89). The confirmation of NGC 5135 group membership is based on spectroscopic observations, in which galaxies with radial velocities outside of $\Delta V \sim 1000$ km s^{-1} are excluded. The KF89 catalogue for the NGC 5135 group consists of a total of seven galaxies. A revision of galaxy groups membership was carried out by Garcia et al. (1993) and Garcia (1993) (hereafter G93) using a combination of friends-of-friends (Huchra & Geller 1982) and Materne-Tully (Materne 1978; Tully 1980) methods. The joint method enables a more reliable way of building a galaxy group catalogue. G93 samples are selected from the Lyon-Meudon Extragalactic Database (Paturel et al. 1988) with cut-offs of *B*-band apparent magnitude of 14.0 and V_{CMB} (recession velocity) ≤ 5500 km s^{-1}. The NGC 5135 galaxy group was then re-grouped as LGG 351 in the G93 catalogue.

LGG 351 consists of 16 galaxies, with 6 galaxies overlapping with the KF89 identification. NGC 5126 is not listed in LGG 351 but a relatively small and nearby galaxy, PGC 46903, is included. Since the *B*-band magnitude of PGC 46903 is fainter than 14.0, it is likely a misidentification of NGC 5126 in G93. We also find that PGC 47574 is a duplicate of PGC 47573 for the given coordinates. In this paper, we consider NGC 5126 instead of PGC 46903 as part of LGG 351 and exclude PGC 47574. We refer readers to G93 for a detailed description of the sample and membership selection criteria. A summary of galaxies in LGG 351 is given in Table 1 and the mean central velocity $\langle cz \rangle$ for LGG 351 is 4146 km s^{-1}.

There are three more galaxy groups in the G93 catalogue that fall within the observed area (see Section 2.1) in different velocity ranges. Among them, the M 83 group is the most interesting. Unfortunately, accurate imaging of M 83 itself was not possible with the early ASKAP-12 array due to limited *UV*-coverage, particularly the lack of short baselines. Instead, LGG 351 is selected for the following reasons: (1) it is one of the main groups of galaxies in the Hydra-Centaurus supercluster (Fouque et al. 1992), thereby allowing the study of 'pre-processing' prior to cluster infall; (2) its stellar mass of $\sim 10^{13}$ $M_\odot$ is higher than previous WALLABY early science studies – NGC 7162 (Reynolds et al. 2019; hereafter R19) and NGC 7232 (Lee-Waddell et al. 2019; hereafter LW19) have group masses of $\sim 10^{12}$ $M_\odot$ – thus extending the range of WALLABY early science studies to higher density environments; (3) it is a loose group that spreads across ~ 10 deg^2 of sky, covering a larger area and a higher redshift range than other WALLABY early science studies (Elagali et al. 2019; LW19; R19; Kleiner et al. 2019), and allowing us to confirm data quality over a wider frequency range.

This paper is structured as follows. Section 2 describes the ASKAP observations, data reduction and data quality. We summarize the source finding methodology and present the H I spectra, moment maps, and associated parameters in Section 3. In Section 4, we revisit group membership. In Section 5, we derive distances, stellar masses, H I masses, and rotational velocities. We compare the derived quantities with scaling relations in Section 6. In Section 7, we derive star formation rates and compare them with star forming main-sequence. Tilted ring fits to the velocity fields and an investigation of H I morphology and environment are presented in Sections 8 and 9. Further

Table 1. Lyon Groups of Galaxies 351.

PGC ID	Other name	RA (J2000) (h:min:s)	Dec. (J2000) ($^{\circ}$:$'$:$''$)	mean V_{hel}[a] (km s^{-1})
46585	ESO 444−G012	13:20:50.5	−29:28:49	4035
46902	NGC 5124	13:24:50.6	−30:18:25	4019
46974	NGC 5135	13:25:44.5	−29:49:59	3866
47078	IC 4248	13:26:47.7	−29:52:58	3902
47169	NGC 5150	13:27:36.6	−29:33:44	4117
47187	NGC 5152	13:27:50.7	−29:37:08	4227
47194	NGC 5153	13:27:54.7	−29:37:08	4068
47573	IC 4275	13:31:51.4	−29:44:01	4240
47489	NGC 5182	13:30:41.3	−28:09:03	4177
47255	ESO 444−G047	13:28:25.1	−31:51:31	4218
46711	ESO 444−G015	13:22:23.6	−31:04:28	4276
46786	ESO 444−G021	13:23:30.3	−30:06:51	4084
46910[b]	NGC 5126	13:24:53.9	−30:19:48	4788
47145	IC 4251	13:27:24.5	−29:26:39	4180
47224	–	13:28:05.7	−29:25:29	3999
47574[c]	–	13:31:51.5	−29:44:02	4109

[a]Mean radial velocity derived from optical and/or H I spectra.
[b]Replacing PGC 46903 from the original G93 catalogue to PGC 46910 due to possible misidentification.
[c]Identified to be a duplicate of PGC 47573.

discussion, summary and conclusions are given in Sections 10 and 11.

Throughout the paper, we adopt a Λ cold dark matter (CDM) cosmological model[1] with $H_0 = 73$ km s^{-1} Mpc^{-1}, $\Omega_m = 0.27$, $\Omega_K = 0$, and $\Omega_{\Lambda} = 0.73$.

2 DATA

2.1 Observations

ASKAP is a radio interferometer (700–1800 MHz) that consists of 36 antennas and has a bandwidth of ∼300 MHz. Each antenna is 12 m in diameter and is equipped with a state-of-the-art MK II phased array feed (PAF). ASKAP is designed to provide high angular and spectral resolution as well as an instantaneous large field of view ($5.5^{\circ} \times 5.5^{\circ}$) with 36 beams for achieving a fast survey speed (Johnston et al. 2007; Hotan et al. 2014; McConnell et al. 2016). An early science program with 12 and, later, 16 MK II PAF-equipped antennas (hereafter ASKAP-12) was conducted during 2016 October to 2018 January. The observations allow us to test the automated data processing software, ASKAPSOFT,[2] assess the data quality, and optimize our data analysis and imaging techniques.

The M 83 field is one of four selected WALLABY early science phase 1 fields, with the majority of the observations taken using 12 antennas. Slightly different antenna array configurations were deployed for the different observations. Sixteen antennas were used in the observation period from 2017 November to 2018 January. A summary of the array configuration for the observations is given in Table 2. We refer the reader to LW19 for the position of these antennas and their assigned number.

The WALLABY early science phase 1 observations were carried out with two interleaving footprints (footprints A and B) with a square 6×6 beam pattern per footprint to achieve uniform RMS. Footprints A and B of the M 83 field are centred on J2000 coordinates $\alpha_A = 13^h37^m54^s$, $\delta_A = -29^{\circ}43'50''$, and $\alpha_B = 13^h39^m58^s.936$, $\delta_B = -30^{\circ}10'46''.36$, respectively. We show the numbering of beams on the footprint in Fig. 1. In Fig. 2, we show the positions of the interleaved footprints with the shaded areas used in this study and the locations of LGG 351 galaxies, respectively.

The observations were carried out mostly during the day, and each observation began with a 2–3 h observation on the primary calibrator, PKS 1934−638. The total integration time on the M 83 field is 160.4 h with ∼135.8 h being used for the data reduction. The observing log is given in Table 3. Each observation is given a scheduling block identification number (SBID).[3]

The M 83 field has also been observed as part of an extragalactic blind survey for very low column density H I (HIDEEP; Minchin et al. 2003). HIDEEP survey was carried out with single-dish 64 m Parkes telescope and covers a total area of $6^{\circ} \times 10^{\circ}$, reaching a column density sensitivity of 7.4×10^{16} cm^{-2} over a 20 km s^{-1} velocity width in the central $4^{\circ} \times 8^{\circ}$ region. LGG 351 is located at the edge of the HIDEEP survey.

2.2 Data reduction

We reduced our data using ASKAPSOFT version 0.20.3. The details of the automated procedure will be published in Whiting et al. (in preparation). The customized procedure that we adopted is described in detailed in (Kleiner et al. 2019) so only a summary is given here. To reduce the processing resources required, we focused on a small range of channels, covering a bandwidth of 20 MHz. We also concatenated data from SBID 4619 and SBID 4620 into one data set.

Table 2. ASKAP early science array configuration for the M 83/LGG 351 field.

Observing period	Antennas	Minimum baseline (m)	Maximum baseline (m)
Dec 2016–Jan 2017	02,04,05,10,12,13,14,16,24,27,28,30	60	2300
Sept 2017	02,03,04,06,10,14,16,17,19,27,28,30	20	2300
Nov 2017–Jan 2018	01,02,03,04,05,06,10,12,14,16,17,19,24,27,28,30	20	2300
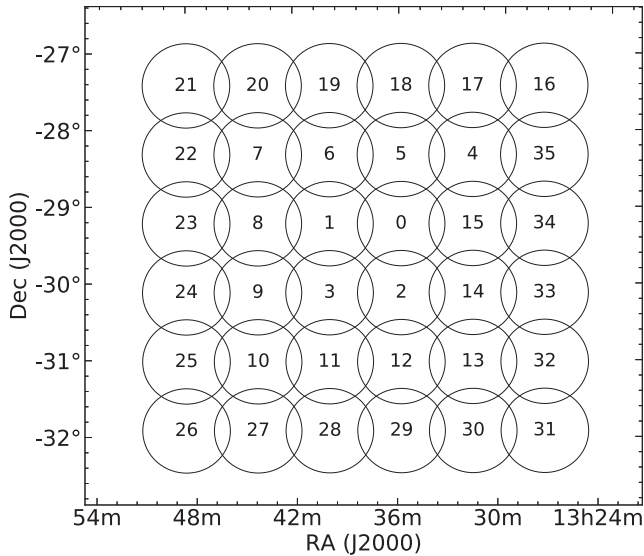
Figure 1. Position and beam number of the ASKAP $6° \times 6°$ square footprint centred on $\alpha_A = 13^h37^m54^s$ and $\delta_A = -29°43'50''$.
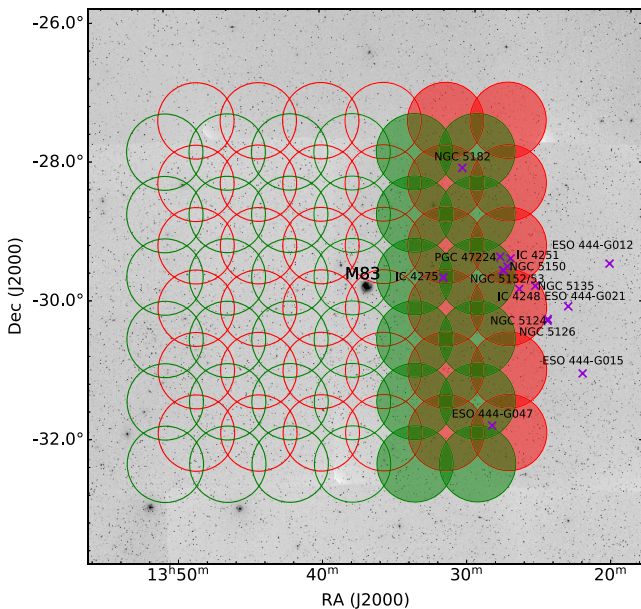
Figure 2. ASKAP footprint overlaid on to the DSS-2 red image centred on M 83. Each beam has an FWHM of $1.0°$ at 21 cm. The red and green represent footprint A and B, respectively. The shaded beams indicate the studied region. The location and name of galaxies in LGG 351 are labelled. Some galaxies are outside the observed footprint.

We ran ASKAPSOFT twice. In the first run, we processed all 36 beams with a 20 MHz bandwidth and stopped at the continuum stage. This yielded a 36-beam mosaicked continuum image per source SB. Each continuum image was used to assess the fluxes, spectral indices and positions of sources by comparing them to the NRAO VLA Sky Survey (NVSS; Condon et al. 1998) and the Sydney University Molonglo Sky Survey (SUMSS; Mauch et al. 2003). This step was required because the early system has phase errors resulting in the phase centres not being exactly at the prescribed positions, which resulted in a small astrometric error of a few arcsec. The offsets for a given SBID were derived from the average offsets of the continuum sources from their true positions. Subsequently, we applied these offsets when we re-ran the full ASKAPSOFT the second time. We only reduced data from beams 4, 13–17, and 30–35 in the second run.

For each source SB, ASKAPSOFT first obtained the footprint information from the observational metadata and converted it to the corresponding beam centre position. Each source SB has an associated calibrator SB, which was used to perform the bandpass calibration. To perform the bandpass calibration, ASKAPSOFT split the calibration data into individual measurement sets (MSs) per beam for the selected channel range. All 36 beams were used for bandpass calibration. These calibration MSs went through autocorrelation, antenna and RFI flagging and were subsequently used to derive the bandpass solution for each beam (refer to Table 3 for flagged antennas).

The source data were also split into individual MS per beam for the selected beams and channel range. The bandpass solution was applied to the source MSs, calibrating the fluxes in each frequency channel by reference to the flux model of PKS B1934−638. Further gain calibration was done through self-calibration, and continuum images for each beam were then created with the calibrated, flagged and spectrally averaged MSs. Each continuum image was used as a model to carry out continuum subtraction in the *UV*-domain. ASKAPSOFT then produced a spectral image cube for each beam. These 'daily' cubes, which could only be cleaned to a shallow level, were used to assess the data quality of each source SB. If an image cube was severely affected by artefacts, its calibrated source MS was excluded in the following customized imaging steps.

Final spectral-line imaging was performed separately using standalone scripts that used tasks in ASKAPSOFT. We first extracted a ~7 MHz sub-MS for each source MS and imaged each selected beam by combining useable sub-MS data (i.e. in the *UV*-domain) using the MSSPLIT and IMAGER tasks, respectively. The key parameters for the imaging included: 4 arcsec pixel^{-1}; Wiener robustness of 0.5; a Gaussian taper of 30 arcsec; and deconvolution with CLEAN using a single scale of one pixel (Högbom 1974). For cleaning, the major-cycle and minor-cycle CLEAN threshold was set to 3σ and 4σ, respectively. One σ corresponds to RMS/$\sqrt{N}$, where RMS is the typical single-night RMS of 7 mJy beam^{-1} and N is the number of combined nights. We created a (spectral-line) image cube per

Table 3. Observing and data reduction log.

UT date (yyyy-mm-dd)	Calibrator SBID	Source SBID	Integration time (h)	Bandwidth (MHz)	Central frequency (MHz)	No. of antennas	Flagged antennas	Notes
Footprint A								
2016-12-24	3017	3014	9.6	192	1344.5	12	16,30	–
2016-12-26	3026	3025	7.5	192	1344.5	12	13,16,30	Partially flagged on 13
2016-12-28	3034	3033	5.6	192	1344.5	12	16,30	–
2016-12-30	3040	3039	10.1	192	1344.5	12	16,24,30	Partially flagged on 24
2017-01-01	3048	3047	8.9	192	1344.5	12	16,30	–
2017-09-23	4372	4371	9.0	192	1368.5	12	–	–
2017-09-27	4396	4387	1.9	192	1368.5	12	–	Not used
2017-09-28	4401	4400	9.0	240	1320.5	16	14	Partially flagged on 14
2017-11-12	4617	4619	3.4	240	1320.5	16	–	Concatenated
2017-11-13	4617	4620	3.0	240	1320.5	16	–	Concatenated
2017-12-15	4831	4830	8.0	240	1320.5	16	–	–
2018-01-03	4928	4931	8.0	240	1320.5	16	–	–
Footprint B								
2016-12-25	3022	3021	6.1	192	1344.5	12	16,30	–
2016-12-27	3030	3029	6.1	192	1344.5	12	16,30	–
2016-12-29	3037	3036	10.0	192	1344.5	12	16,24,30	Partially flagged on 24
2016-12-31	3045	3044	8.6	192	1344.5	12	16,30	–
2017-01-02	3051	3050	8.4	192	1344.5	12	16,30	–
2017-09-24	4377	4376	9.0	192	1368.5	12	–	–
2017-09-26	4388/4383	4382	4.5	192	1368.5	12	–	–
2017-09-29	4405	4403	2.7	240	1320.5	12	–	Not used
2017-11-14	4617	4623	7.0	240	1320.5	16	–	–
2017-12-16	4836	4835	6.0	240	1320.5	16	–	–
2018-01-04	4936	4935	8.0	240	1320.5	16	–	–

beam. Subsequently, the residual continuum emission in the cube was removed by fitting a low-order polynomial to each spectrum. This yielded 12 image cubes per footprint and 24 image cubes in total. Finally, we mosaicked image cubes using the LINMOS task, where the primary beam correction was also applied. The image cube of beam 31 (footprint B) was excluded from the mosaic due to severe artefacts caused by solar interference (see Section 2.3). Excluding short baselines to mitigate against solar interference was avoided so as not to miss out on extended emission.

The final mosaicked cube covers a frequency range in the barycentric frame of 1396.57–1403.56 MHz (corresponding to V_{opt} = 3599.1–5115.8 km s^{-1}) and has a synthesized beam of 45 arcsec × 35 arcsec.

2.3 Data quality assessment

Statistical analysis was performed on the combined image cubes to assess the data quality of the ASKAP-12 data. RMS flux density values per channel per beam were measured. We find average RMS values of 2.2 and 2.6 mJy for beams in footprint A and B, respectively. These values are slightly better than the theoretical RMS of ~2.8 mJy for the given on-source integration time (assuming T_{sys}/η of 75 K).

To characterize the distribution of noise in our image cubes, we examined the distribution of flux values for all voxels in each cube and calculated 1 and 99 percentile values of the distribution. The distribution of the noise is well represented by a Gaussian. The noise level can also be characterized by the 1 percentile rank of the pixel flux distribution to avoid bias by the contribution from the H I sources (see e.g. Wong et al. 2006). In Fig. 3, we show the map of 1 percentile noise levels for beams in footprints A and B. Higher negative values indicate excessive negative flux, which is due to
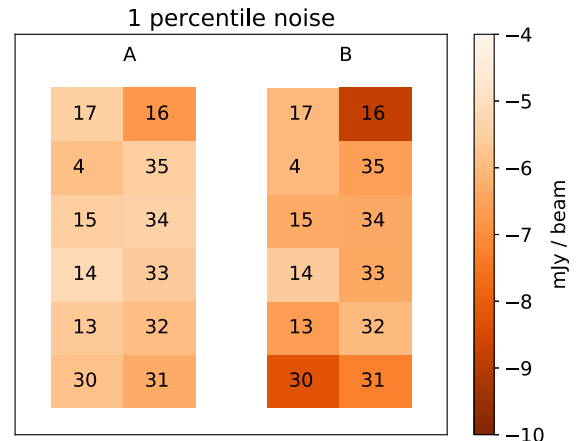

Figure 3. 1 percentile rank noise levels for combined beam image cubes of both footprints. Darker, negative values indicate issues with bandpass calibration, sensitivity drop off for corner beams and/or negative sidelobes. The text in each rectangle represents beam number.

issues with bandpass calibration, sensitivity drop off towards corner beams and/or negative sidelobes. The data quality of footprint A is better than B.

Observations of the field were planned to avoid certain angles from the Sun in order to minimize solar interference. However, image stripes, which are a signature of solar interference, are seen in some of our image cubes. We find that they are better characterized by the maximum flux density. In Fig. 4, we show the maximum flux density as a function of frequency for beams 14 and 31 in footprint A and beam 31 in footprint B. The RMS values do not show such difference or variation with frequency, but the maximum
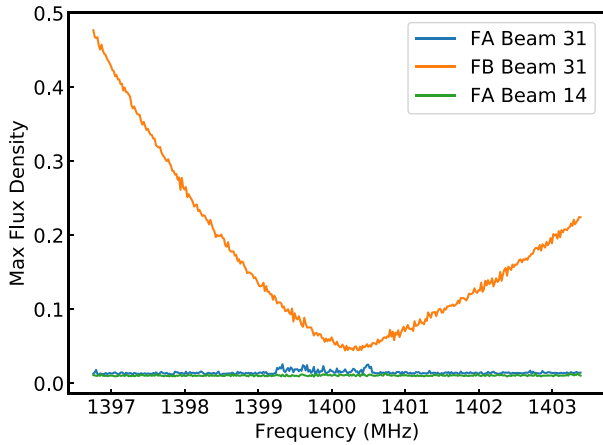
Figure 4. Maximum flux density (Jy) as a function of frequency for the beam 14 and 31 image cubes in footprint A and the beam 31 data cube in footprint B. There is a significant variation in max flux density caused by the solar interference.

flux density in beam 31 for footprint B varies significantly by $\sim$0.4 Jy across the whole frequency range. Using the maximum flux density as a metric, we identify the SBID 4623 data set as the main contributor to the stripes. This observation was carried out closest to the Sun, with beam 31 located at a Sun angle of $40°$.

3 SOURCE FINDING AND CATALOGING

We search for H I sources in the mosaicked cube using the Source Finding Application (SOFIA;[4] Serra et al. 2015). SOFIA is developed with ASKAP and future H I surveys in mind. WALLABY early science data are well suited to test SOFIA and to aid improving its algorithms. For the input parameters, we set a sub-cube region to exclude the first and last 10 channels due to low signal to noise (S/N) in these channels that do not contain all the combined data due to Doppler corrections. We use the local RMS for the noise scaling and a 5σ threshold for the smooth + clip source detection algorithm. We merge detected voxels into objects with a merging radius of 8 pixels and five spectral channels, and apply mask dilation for all detected sources to recover their total H I flux.

SOFIA generates outputs of individual cubelets and associated mask cubes for detected sources. For each source, a spectrum, integrated H I intensity (0th moment), velocity field (1st moment), velocity dispersion (2nd moment), and position–frequency maps are also generated based on the mask cube. To verify the detected sources, we follow these steps:

(i) Overplot the source positions on to images of the same region from the NVSS and the SUMSS to identify incomplete continuum subtraction. It was a known issue with this version of ASKAPSOFT that bright continuum sources ($\gtrsim$0.5 Jy) are unlikely to be subtracted completely.

(ii) Cross match with the NED and SIMBAD databases (Wenger et al. 2000). The search radius is first set to 45 arcsec and then 60 arcsec if no source is found within 45 arcsec ($\sim$1 synthesized beam size).

(iii) Check the remaining detections by eye using the corresponding cubelet, 0th and 1st moment maps. A genuine detection generally has a coherent structure and velocity field. If selected, we further cross check them with optical images.

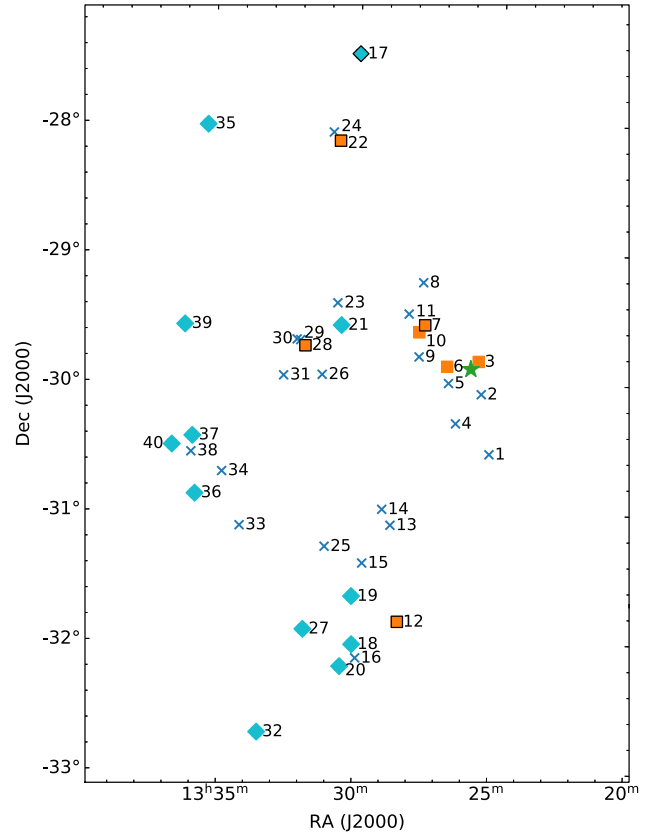[4]Available at https://github.com/SoFiA-Admin/SoFiA

Figure 5. The on-sky distribution of all 40 detected H I sources with numbers corresponding to the ID in Tables 4 and 5. Orange squares and those with black edges are galaxies in LGG 351 from the G93 catalogue and from the HIDEEP catalogue, respectively. Blue crosses and light-blue diamonds represent the surrounding galaxies. The light-blue diamond with black edge is the interacting pair, which is also unresolved in the HIDEEP catalogue. New group members are discussed in Section 4. The centre of the galaxy group as defined by Tully (2015) is shown as a green star.

The final catalogue consists of 40 H I sources, which includes a newly identified tidally interacting galaxy pair (WALLABY J133002−272832) and two sources (WALLABY J133201−294119 and WALLABY J133237−295743) that do not have optical identifications. There are 15 galaxies in LGG 351 with five outside the footprint coverage area. Seven of the remaining 10 galaxies have H I detections. The on-sky distribution of 40 H I sources with their numbering is shown in Fig. 5. There are a few partial H I detections (e.g. only half of the double-horn profile is detected), which is due to the detection limit of the survey and/or higher noise at the edge of the beam where the source is located. We will exclude the tidal interacting galaxy pair and partial H I detections from the following statistical analysis, leaving a tally of 36 H I detections. There are only 5 and 16 of them detected in HIPASS and HIDEEP, respectively. The properties and parameters of each source are given in Tables 4 and 5. The derivation of parameters is described in the following sections.

3.1 H I spectra and integrated flux

SOFIA extracts the spectrum of each source by integrating the flux densities of all spatial pixels in each spectral channel. We plot the spectra in the optical velocity frame , $V_{opt} = cz$, where c is the speed of light and z is the redshift. The integrated flux (S_{int}) is then the integral of the flux densities of all channels in the spectrum. We

Table 4. Source catalogue and derived parameters.

ID	Designation	Other ID	α (J2000) (°)	δ (J2000) (°)	ν_{obs} (MHz)	z	V_{opt} (km s^{-1})	V_{CMB} (km s^{-1})	D_H (Mpc)	D_L (Mpc)	$N_{HI,sen}$ ($\times 10^{19}$ cm^{-2})	S_{int} (Jy Hz)	$\log M_{HI}/M_\odot$
(1)	(2)	(3)	(4)	(5)	(6)	(7)	(8)	(9)	(10)	(11)	(12)	(13)	(14)
1	WALLABY J132514−303304*	ESO 444−30	201.30863	−30.55121	1400.2776	0.0144	4309	4597	63.0	63.9	7.0	>3790.2	>8.89
2	WALLABY J132533−300521	LEDA 721502	201.39069	−30.08933	1399.8200	0.0147	4409	4697	64.3	65.3	4.0	2576.1	8.74
3	WALLABY J132541−295013*	NGC 5135	201.42083	−29.83698	1401.2469	0.0137	4099	4388	60.1	60.9	7.0	>12113.1	>9.35
4	WALLABY J132627−301909	LEDA 718624	201.61538	−30.31931	1399.9614	0.0146	4378	4666	63.9	64.8	4.8	4199.9	8.94
5	WALLABY J132644−300031	FLASH J132644.53−300029.9	201.68581	−30.00881	1401.5354	0.0135	4036	4324	59.2	60.0	3.7	3028.9	8.73

Note. This table is available in its entirety as Supporting Information with the electronic version of the paper. A portion is shown here for guidance regarding its form and content. Cols (1)–(3): identification, designation, and other identification, respectively. Cols (4)–(5): α and δ (J2000) coordinates are based on the H I detection. Col (6): ν_{obs} – the detected central frequency of the source. Col (7): z is redshift, defined as $z = (\nu_{rest} - \nu_{obs})/\nu_{obs}$, where ν_{rest} is H I rest frequency at 1420.405751 MHz and ν_{obs} is observed frequency. Col (8): $V_{opt} = cz$ – velocity in the optical reference frame. Cols (9)–(11): V_{cos}, D_H, and D_L – recession velocity, Hubble distance, and luminosity distance, respectively (see Section 5.1). Col (12): $N_{HI,sen}$ – 1σ H I column density sensitivity (see Section 3.2). Col (13): $S_{int} = \sum S \times \Delta\nu$ – integrated flux (see Section 3.2). Col (14): $\log M_{HI}/M_\odot$ – observed H I mass in logarithmic scale (see Section 5.2).
*Partial H I detection.
†Tidally interacting pair.

Table 5. 2MASS K_s-band photometry, physical properties of sources, and relevant derived parameters.

ID	Designation	$E(B-V)$ (mag)	K_s (mag)	errK_s (mag)	F_{K_s} (Jy)	νL_ν ($\times 10^9$ L$_\odot$)	$\log M_*/M_\odot$ (M$_\odot$)	Morphology	d_{25} (kpc)	DEF$_{HI}$	i (°)	w_{20}^c (km s^{-1})	V_{rot} (km s^{-1})
(1)	(2)	(3)	(4)	(5)	(6)	(7)	(8)	(9)	(10)	(11)	(12)	(13)	(14)
1	WALLABY J132514−303304*	0.0561	10.600	0.034	0.038	6.79	10.2	Sa	20.5	−	69	57.6	−
2	WALLABY J132533−300521	0.0552	−	−	−	−	−	−	−	−	−	44.4	−
3	WALLABY J132541−295013*	0.0517	8.811	0.032	0.199	32.07	10.9	SBab	45.6	−	63	113.4	−
4	WALLABY J132627−301909	0.0545	−	−	−	−	−	−	−	−	−	121.1	−
5	WALLABY J132644−300031	0.0520	−	−	−	−	−	dwarf?	−	−	−	85.0	−

Note. This table is available in its entirety as Supporting Information with the electronic version of the paper. A portion is shown here for guidance regarding its form and content. Cols (1) and (2): Identification and designation, respectively. Col (3): $E(B-V)$ – Galactic dust extinction (Schlafly & Finkbeiner 2011, see Section 5.2.1). Cols (4)–(6): K_s, errK_s, and F_{K_s} – intrinsic magnitude, error, and intrinsic flux density in 2MASS K_s band, respectively (see Section 5.2.1). Col (7): νL_ν – luminosity in 2MASS K_s band. Col (8): $\log M_*/M_\odot$ – derived stellar mass in logarithmic scale (see Section 5.2.1). Col (9): Morphology – retrieved from NED or SIMBAD. Col (10): Calculated B-band optical isophotal diameter measured at 25 mag arcsec^{-2} – $d_{25} = D_L \tan(B_{25,maj})$, where $B_{25,maj}$ is homogenized major axis from NED (see Section 5.2.2). Col (11): DEF$_{HI}$ – H I deficiency (see Section 5.2.2). Col (12): i – inclination as given by minor/major axial ratio to 3σ in 2MASS K_s band. Cols (13)–(14): w_{20}^c and V_{rot} – corrected w_{20} linewidth provided by SoFiA and calculated rotational velocity from the H I linewidth, respectively (see Section 5.3).
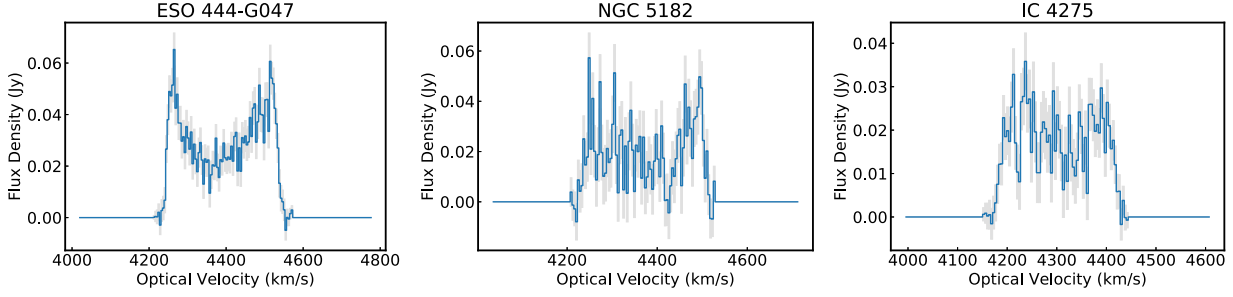*Partial H I detection.
†Tidally interacting pair.

Figure 6. Examples of spectra of individual sources derived by SOFIA. Local RMS is shaded in grey. *Note*. This figure is published in its entirety as Supporting Information with the electronic version of the paper. A portion is shown here.
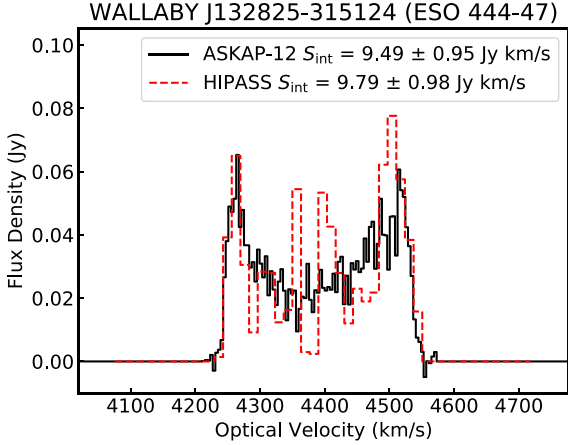

Figure 7. Comparison between ASKAP-12 (black) and HIPASS 1328−31 (red) spectra of WALLABY J132825−315124 (ESO 444−47). Both spectra are extracted with SOFIA for direct comparison. The integrated fluxes are in agreement with each other.
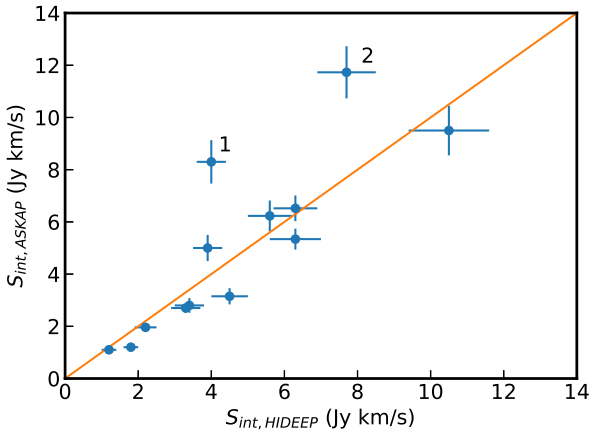

Figure 8. Comparison of ASKAP-12 and HIDEEP integrated fluxes (Minchin et al. 2003). The red line indicates equality of integrated fluxes. Outliers are labelled numerically and discussed in Section 3.1.

keep S_{int} in the original physically correct units of Jy Hz instead of the traditional Jy km s^{-1} unit because Jy km s^{-1} is a 'pseudo-flux' unit that is ambiguous beyond $z \sim 0.1$ (Meyer et al. 2017; hereafter M17). In Fig. 6, we show spectra of sources extracted by SOFIA and note that some of them have low S/N ratio, or have only partial H I detections.

To verify the measured integrated fluxes from the ASKAP-12 data, we compare the spectra and integrated fluxes of a common (iso-lated) H I source between our study (WALLABY J132825−315124) and HIPASS (HIPASS 1328−31). For direct comparison, we extract the spectrum from the HIPASS sub-cube in the same way as we do for WALLABY J132825−315124. As shown in Fig. 7, the integrated fluxes in this case are consistent with each other.

We also compare the fluxes from ASKAP-12 with HIDEEP measurements in Fig. 8, where two outliers (labelled 1 and 2) are noted. We find that ASKAP source, IC 4290 (point 1), falls within the same beam as a single HIDEEP source (HIDEEP J1335−2801). Within the two overlapping beams of HIDEEP J1335–3025 and HIDEEP J1336−3030, there are three resolved ASKAP sources, namely ESO 444−77, 2MFGC 10975, and LEDA 715863. The value of $S_{int,ASKAP}$ for 2MFGC 10975 (1.1 ± 0.1 Jy km s^{-1}) is consistent with $S_{int,HIDEEP}$ (1.8 ± 0.2 Jy km s^{-1}). LEDA 715863 is not resolved by the HIDEEP survey and the flux contribution to the total $S_{int,ASKAP}$ is relatively small (0.6 ± 0.1 Jy km s^{-1}). The main deviation comes from the measured integrated fluxes of ESO 444−77. Examining the ASKAP-12 and HIDEEP cubes, we find that these sources are located in an area where S/N is low and only data from footprint B are present in the mosaicked cube. As mentioned in Section 2.3, the effect of solar interference is prominent in these beams, which may have resulted in additional flux. We should also point out that spectra of HIDEEP J1335−2801 and HIDEEP J1335–3025 reveal obvious baseline ripple, which can also affect the accuracy of integrated fluxes.

3.2 H I intensity and velocity field maps

We convert the H I intensity maps in units of Jy Hz from SOFIA to H I column density ($N_{H I}$) using equation 76 in M17:

$$\left(\frac{N_{H I}}{cm^{-2}}\right) = 2.33 \times 10^{20}(1 + z)^4 \frac{S}{Jy\ Hz}\left(\frac{ab}{arcsec^2}\right)^{-1}, \qquad (1)$$

where $N_{H I}$ is the H I column density and a and b are beam angular major and minor axes, respectively. To better overlay a common set of contour levels on to optical images, we use H I column density sensitivity ($N_{H I,sen}$) levels. In Fig. 9, we show the ASKAP $N_{H I,sen}$ contours overlaid on to an optical r-band Digital Sky Survey 2 (DSS2r) or a combined g and r-band Dark Energy Camera (DECam) image for all detected sources. DECam images are at higher resolution than DSS2r, hence preferred wherever available. The contour levels are 3, 5, 7, 9, 11, and 13 times $N_{H I,sen}$, where $N_{H I,sen}$ is given by

$$\left(\frac{S_{H I,sen}}{Jy\ Hz}\right) = \sigma_{RMS} \times \sqrt{N_{chan}} \times \Delta\nu, \qquad (2)$$
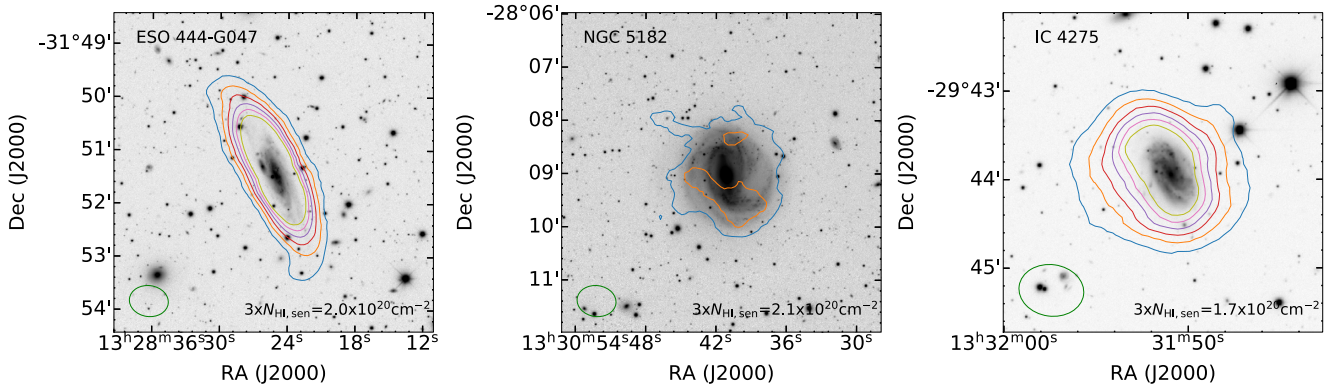
Figure 9. Examples of integrated H I column density maps of individual sources overlaid on to DSS2r or DECam (Müller, Jerjen & Binggeli 2015) images. The contour levels are 3, 5, 7, 9, 11, and 13 × $N_{H I,sen}$ in cm^{-2}, (refer Table 4), which corresponds to colour scale of blue, orange, red, purple, pink, and olive green, respectively. The synthesized beam of 45 arcsec × 35 arcsec is plotted at the bottom left corner of each sub-plot as a reference. *Note*. This figure is published its entirety as Supporting Information with the electronic version of the paper. A portion is shown here.
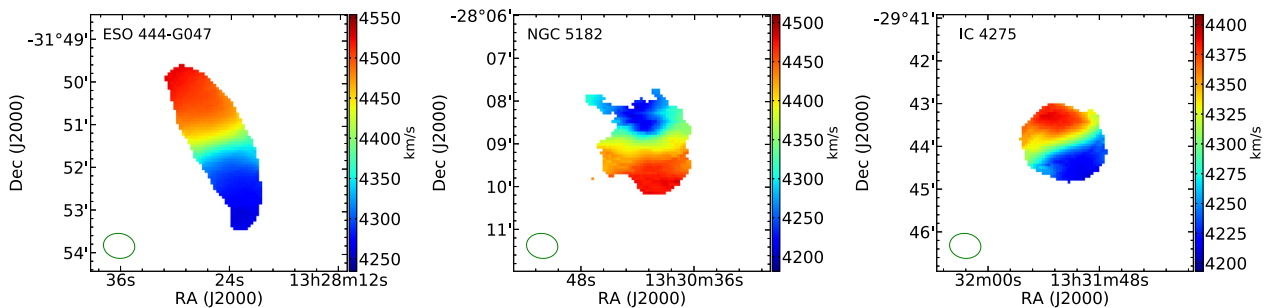

Figure 10. Examples of velocity field maps of individual sources, where only pixels above 3 × $N_{H I,sen}$ are plotted. The synthesized beam of 45 arcsec × 35 arcsec is plotted at the bottom left corner of each sub-plot. *Note*. This figure is published its entirety as Supporting Information with the electronic version of the paper. A portion is shown here.

where σ_{RMS} is the local RMS in Jy, N_{chan} is the total number of channels that contain H I emission and Δv is the channel width of ASKAP data. Then, the conversion from flux density (sensitivity) to $N_{H I}$ (sensitivity) is given in equation (1). This gives an upper limit for $N_{H I,sen}$ because not all pixels contain the same number of channels with H I emission.

In Fig. 10, we present the 1st moment velocity field maps of all sources. Pixels below 3 × $N_{H I,sen}$ are masked out. We note that most of the detected galaxies are marginally resolved.

4 GROUP MEMBERSHIP

Galaxy group membership depends strongly on the selection criteria and algorithms. While the G93 catalogue is constructed with a combination of methods, it is limited to magnitude ($B_{mag} < 14.0$) and only to the nearby Universe ($V_{CMB} \leq 5500$ km s^{-1}). More recent studies of galaxy group membership have been carried out by Yang et al. (2007), who used SDSS (York et al. 2000) and 2dFGRS (Colless et al. 2001) data, with vastly more spectroscopic redshifts compared with G93. Tully et al. (2013) has also constructed a galaxy group catalogue based on a compilation of distances and peculiar velocities of >8000 galaxies. Both Yang's and Tully's catalogues are constructed with different selection criteria and scientific goals, and are not directly comparable.

Given that the H I detected galaxies in our study are close in projected separation and in velocity to the existing galaxies defining LGG 351 (see Fig. 5), they are likely to all be members of an

extended group. To determine if associated with LGG 351, we calculate the velocity difference between each galaxy and the mean central velocity of LGG 351 ($\Delta V = V_{opt} - \bar{V}$) and then compare it to $3\sigma_{vel}$. With this criterion, we exclude IC 4290 from being part of the group. Re-iterating with the new $\bar{V}$ and σ_{vel}, we do not find any other exclusions. Many of the detected H I sources have also been identified as part of the TSK group 2543 (Tully et al. 2008, 2013). This part of the local Universe is markedly overdense, due to being within the extended Hydra-Centaurus supercluster.

4.1 Dwarf galaxies

Dwarf galaxies play an important role as they are the building blocks of galaxies. In the context of H I, dwarf galaxies in the Local Group as well as the newly discovered satellites of the Milky Way and the Andromeda galaxy are H I deficient (Grcevich & Putman 2009; Westmeier et al. 2015). This is in part due to tidal and ram-pressure effects in the vicinity of massive galaxies in the Local Group. The discovery of gas-rich ultra-faint dwarf galaxies, such as Leo P (Giovanelli et al. 2013; McQuinn et al. 2015) suggests that the census of dwarf satellites remains incomplete due to sensitivity limitations of instruments at both in optical and radio wavelengths.

A search for ultra-faint dwarf galaxies with DECam down to $M_v \sim -10$ mag has been conducted in the vicinity of the Centaurus group, which consists of the Centaurus A and M 83 subgroups (Müller
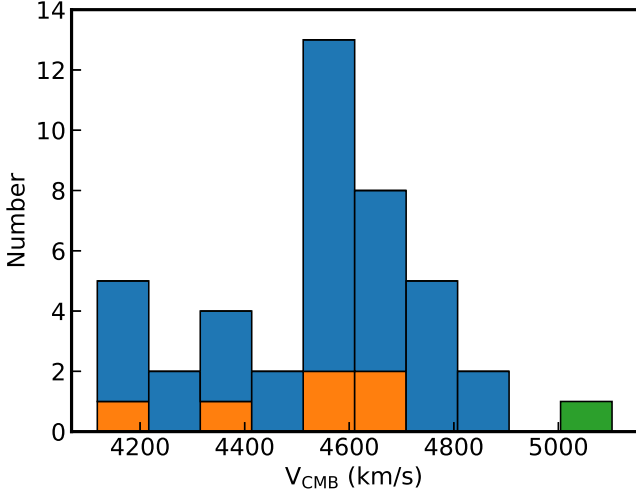
Figure 11. Histogram of recession velocities (V_{CMB}). Orange and blue represent galaxies in G93 LGG 351 catalogue and the newly identified galaxies, respectively. IC 4290, which is probably not a group member is represented in green.
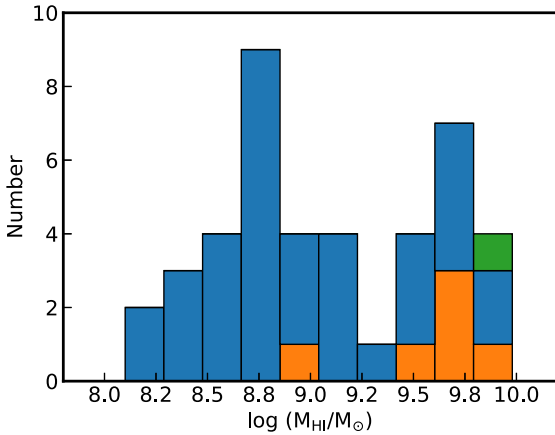

Figure 12. Histogram of H I masses. Orange and blue represent galaxies in G93 LGG 351 catalogue and the newly identified galaxies, respectively. Two peaks are seen in this distribution, with one at the low-mass end and the other at the high-mass end. IC 4290 is represented in green.

et al. 2015; Müller, Jerjen & Binggeli 2017). They find 41 new dwarf galaxy candidates, which nearly doubles the number of known galaxies in the Centaurus group. Confirmation of their membership relies on the tip of the red giant branch distance measurements and the surface brightness fluctuation method (Tonry & Schneider 1988), but only a handful of them have been measured to date (Müller, Rejkuba & Jerjen 2018).

The H I spectral line provides another way to estimate distances (see Section 5.1) if these ultra-faint dwarf galaxies contain H I. Analysis of HIPASS data shows no H I detection and gives an upper limit of $M_{HI} < 8.5 \times 10^6$ M$_\odot$ to these dwarf galaxy candidates (Müller et al. 2017). Nevertheless, we search for an H I signature of some of these ultra-faint dwarf galaxies given that they fall within the studied area. We find a detection of H I for dw 1328−29 (#11), which has M_{HI} of 3.4×10^8 M$_\odot$ and is at the low end of H I masses of galaxies within LGG 351 (see Fig. 12). This also rules out dw

1328−29 as a member of the M 83 group. We also identify LEDA 98614 (#14) as a dwarf candidate based on the combined *g* and *r*-band DECam image.

5 PHYSICAL PARAMETERS

5.1 Luminosity and Hubble distances

We calculate the Hubble distance (D_H), which is defined as $D_H = V_{CMB}/H_0$, where

$$V_{CMB} = V_{opt} + V_{apex} \left[\sin b \sin b_{apex} + \cos b \cos b_{apex} \cos(l - l_{apex}) \right] \quad (3)$$

is the recession velocity in the cosmic microwave background (CMB) reference frame, $l_{apex} = 264.14°$, $b_{apex} = 48.26°$, and $V_{apex} = 371.0$ km s^{-1} (Fixsen et al. 1996). Galactic coordinates of galaxies are represented by l and b. We can also calculate the luminosity distance, $D_L = (1 + z)D_c$, where D_c is the co-moving distance. At low redshift, $D_c \approx D_H$. In Fig. 11, we show the V_{CMB} distribution of H I detected galaxies in the field. The distribution peaks at ∼4600 km s^{-1} and the mean LGG 351 V_{CMB} is 4500 km s^{-1}, which corresponds to a mean D_L of 63.2 Mpc.

5.2 Masses

5.2.1 Stellar mass

Stellar masses can be derived by using colour–mass relations. Near-infrared (NIR) luminosities of galaxies are useful for estimating the mass-to-light ratio (*M/L*) as they only vary slightly across a wide range of star formation histories (Bell & de Jong 2001; Bell et al. 2003). To make use of the existing NIR colour–stellar mass relations, we first obtain the K_s colours of our galaxies from the 2MASS extended source catalogue (Skrutskie et al. 2006). Using the wavelength-dependent extinction law of Cardelli, Clayton & Mathis (1989), we derive $A_{K_s} = 0.36 E(B - V)$. The Galactic dust extinction, $E(B - V)$, of each galaxy is estimated using the re-calibrated SFD all-sky extinction maps (Schlegel, Finkbeiner & Davis 1998; Schlafly & Finkbeiner 2011). Following the procedure as described in section 6 of For, Koribalski & Jarrett (2012), we obtain the intrinsic fluxes in the K_s band by adopting the zero-magnitude flux of the star Vega (F_0). The corresponding F_0 is 666.7 ± 12.6 Jy (Cohen, Wheaton & Megeath 2003). We also estimate the k-correction for the K_s band (Chilingarian, Melchior & Zolotukhin 2010; Chilingarian & Zolotukhin 2012), which ranges from −0.03 to −0.05 mag. The correction is smaller than a typical K_s mag error of 0.09 and hence is considered to be negligible. Subsequently, we obtain the stellar masses by employing the 2MASS K_s band to stellar mass relation as given in equation 3 of Wen et al. (2013):

$$\log \left(\frac{M_*}{M_\odot} \right) = (-0.498 \pm 0.002)$$
$$+ (1.105 \pm 0.001) \log \left(\frac{\nu L_\nu}{L_\odot} \right). \quad (4)$$

This relation uses the Salpeter (1955) IMF. For comparing with the literature, where the Chabrier (2003) IMF is commonly used, we scale the M_* values by a factor of 0.61 (Madau & Dickinson 2014). Stellar masses of galaxies in our study are of the order of $10^{8.5-11}$ M$_\odot$.
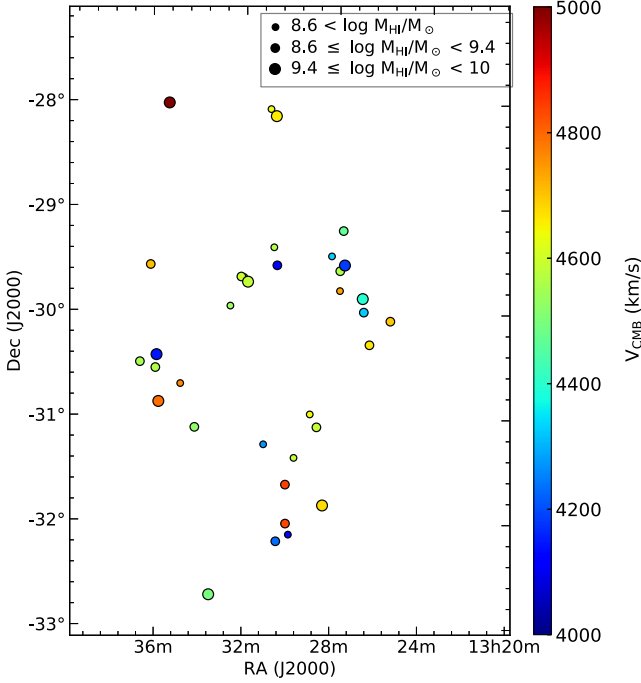
Figure 13. The on-sky distribution of 36 detected H I sources with colour and size corresponds to V_{CMB} and H I masses, respectively.

5.2.2 H I mass and the H I-deficiency parameter

Assuming the H I sources are optically thin, we use a simplified version of equation 48 in M17 to calculate the H I mass,

$$\left(\frac{M_{HI}}{M_\odot}\right) \simeq 49.7 \left(\frac{D_L}{Mpc}\right)^2 \left(\frac{S_{int}}{Jy\ Hz}\right), \quad (5)$$

where D_L is the luminosity distance and S_{int} is the integrated flux. Fig. 12 shows the distribution of H I mass, which has a range of $\sim 10^{8-10}\ M_\odot$ and a median of $\log M_{HI}/M_\odot = 8.87$. Galaxies in LGG 351 from the G93 catalogue generally have H I masses $>10^9\ M_\odot$. We also show the sky distribution of the 36 detected H I sources with colour and size corresponding to V_{CMB} and H I mass, respectively (Fig. 13). There is no obvious trend in the velocity distribution. The majority of the most massive galaxies are in close projected separation to less massive galaxies.

We can assess the 'richness' of H I masses of our galaxies by comparing them to the expected H I masses. To quantify it, an H I-deficiency parameter, DEF_{HI}, is introduced by Haynes & Giovanelli (1984). DEF_{HI} is defined as the logarithmic difference between the expected and observed H I masses of a galaxy,

$$DEF_{HI} = \frac{\log M_{HI,exp}}{M\odot} - \frac{\log M_{HI,obs}}{M_\odot}. \quad (6)$$

The expected H I mass of each galaxy is determined by its morphology and size,

$$\log\left(\frac{M_{HI,exp}}{M_\odot}\right) = a_{HI} + 2 \times b_{HI} \times \log\left(\frac{hd_{25}}{kpc}\right) - 2\log(h), \quad (7)$$

where a_{HI} and b_{HI} are coefficients based on Hubble morphological types (Solanes, Giovanelli & Haynes 1996; refer to table 3 in Boselli & Gavazzi 2009), $h = H_0/100$ km s^{-1} Mpc^{-1} and d_{25} is the optical isophotal diameter measured at 25 mag arcsec^{-2} in B-band. Following the definition in Cortese et al. (2011), we consider a galaxy to be H I deficient when $DEF_{HI} \geq 0.5$ and to be H I excess

when $DEF_{HI} \leq -0.5$. These correspond to 70 per cent less or more H I as compared to isolated galaxies of the same morphological type and diameter.

We obtain the morphological type and calculate the D_{25} based on the B_{25} semimajor axis (B_{maj}) from NED. There are only 11 galaxies in our study with available morphological classifications, B_{maj} measurements and H I masses. Among them, NGC 5152 (DEF_{HI} = 0.98) and ESO 444−G047 (DEF_{HI} = −0.56) are considered H I deficient and H I excess. The finding is similar to the NGC 7162 group, in which majority of the group members are H I normal with one galaxy (ESO 288−G025) being H I deficient (DEF_{HI} = 0.50) (R19[5]). However, we note that our sample is small for statistical interpretation.

A recent study on H I scaling relations derived from isolated galaxies, which may not be strongly affected by the environment, is described in Jones et al. (2018). The samples are drawn from the Analysis of the interstellar Medium of Isolated GAlaxies project (AMIGA; Verdes-Montenegro et al. 2005) and are divided into three morphological types (early-type, late-type, and very late-type galaxies). The derived coefficient (b as in equation 7) for the late-type galaxies in this study is larger than in Solanes et al. (1996) but is more consistent with the study of Haynes & Giovanelli (1984). The difference may indicate an influence on environment. We refer the readers to Jones et al. (2018) for a detailed comparison and discussion of different H I scaling relations and note that the derived scaling relations are subject to the selection effects.

5.3 Rotational velocity

The rotational velocity of a galaxy can be calculated from the H I linewidth, as given by

$$V_{rot}\ (km\ s^{-1}) = \frac{w_{20}^c}{2\sin i}, \quad (8)$$

where $w_{20}^c = \sqrt{w_{20}^2 - (\Delta s)^2}$ is the H I linewidth measured at 20 per cent of the level of each peak, and corrected for instrumental broadening (Δs) and i is the inclination. According to Springob et al. (2005), $\Delta s = 2\Delta v\lambda$, where Δv is assumed to be equal to, or close to, the channel width in velocity space, and λ is the broadening parameter. We adopt $\lambda = 0.5$, which is appropriate for typical profile shapes. We can compute the inclination using the following equation:

$$\cos i = \sqrt{\frac{(b_{min}/b_{maj})^2 - q^2}{1 - q^2}}, \quad (9)$$

where b_{min}/b_{maj} is the axial ratio of minor-to-major axes from 2MASS K_s band and q is the intrinsic axial ratio. We adopt a constant q of 0.2 (Tully et al. 2009) because the difference in q values is small between different morphological types (see discussion in Catinella et al. 2012; hereafter C12). The calculated V_{rot} are given in Table 5.

6 COMPARISON WITH SCALING RELATIONS

A series of studies on H I scaling relations have been carried out as part of the *GALEX* Arecibo SDSS Survey (GASS; see Catinella et al. 2013 and references therein) and extended GASS (xGASS;[6] see Catinella et al. 2018 and references therein). GASS

---

[5]For consistency, we revise their calculation and find that those galaxies previously reported to be H I excess are H I normal.
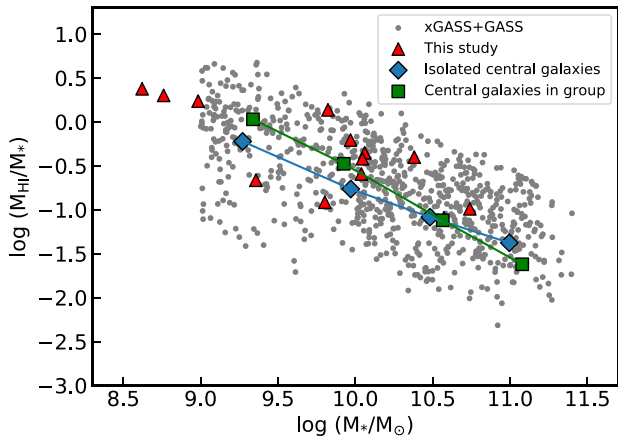[6]http://xgass.icrar.org/data.html

Figure 14. Measurements in this study overlaid (filled red triangles) on to GASS and xGASS (grey dots) galaxies as a function of stellar mass. Neither GASS nor xGASS samples cover the low stellar mass regime ($\log M_*/M_\odot < 9.0$).

is a large Arecibo H I survey that targets galaxies with stellar masses greater than 10^{10} $M_\odot$ and redshifts $0.025 < z < 0.05$. xGASS is an extension of GASS to include lower stellar mass galaxies ($10^9 < M_* < 10^{11.5}$ $M_\odot$) and redshifts $0.01 < z < 0.05$. In this section, we compare our derived parameters to H I scaling relations.

6.1 Atomic gas fraction scaling relation

The atomic gas fraction (M_{HI}/M_*) varies as a function of integrated galaxy properties and decreases with M_*. Massive galaxies ($M_* > 10^{10}$ $M_\odot$) within large haloes ($M_h = 10^{13}$–$10^{14}M_\odot$) have less H I gas fractions than those galaxies with similar M_* in smaller haloes (Catinella et al. 2013). In Fig. 14, we overplot our data (red triangles) on to the atomic gas fraction scaling relation that is based on the GASS and xGASS data (grey circles). The average atomic gas fraction of isolated central galaxies (blue diamonds) and central galaxies in group (green squares) from the study of Janowiecki et al. (2017) is also shown. They find that the average gas fraction in central galaxies in group below $10^{10.2}$ $M_\odot$ is ~0.3 dex higher than isolated central galaxies. The majority of our galaxies ($M_* > 10^9$ $M_\odot$) are above the green line, which consistent with the Janowiecki's result. It is unclear if the discrepancy of gas fraction between isolated central galaxies and central galaxies in group remains below 10^9 $M_\odot$. Further investigation is needed.

However, examining the atomic gas fraction scaling relation that is derived from the Herschel Reference Survey (HRS; Boselli et al. 2010), which covers stellar masses below 10^9 $M_\odot$ (see fig. 1 in Cortese et al. 2011), we find that the low-mass galaxies in this study follow the same general trend. The two low stellar-mass galaxies, WALLABY J133035−293421 and 2MFGC 10975 with $\log M_{HI}/M_* > 0$, indicate that gas is inefficiently converting into stars.

6.2 Baryonic Tully–Fisher relation

The baryonic mass is the sum of gas and stellar masses, in which the total gas mass is mostly composed of molecular and neutral hydrogen. The contribution from H_2 is small for the range of stellar masses being studied in C12. As such, we use $M_{gas} = 1.4 M_{HI}$, where a 1.4 correction factor is applied to account for helium and
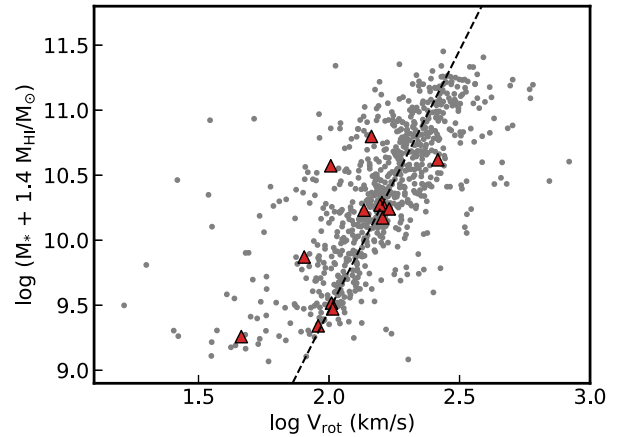

Figure 15. Measurements in this study (filled red triangles) overlaid on to GASS and xGASS (grey dots) galaxies for the BTF relation. The dashed line represents the fit from C12.

metals. In Fig. 15, we overplot our data (filled red triangles) on to the GASS and xGASS data (grey circles) for the Baryonic Tully–Fisher (BTF) relation. The dashed line represents the fit from C12. We find that V_{rot} for five galaxies (2MFGC 10975, NGC 5152, IC 4290, NGC 5150, and NGC 5182) deviates by more than 0.1 dex from the fitted BTF scaling relation. However, we note that the scatter for the C12 samples is 0.127 dex, with a smaller scatter of 0.076 dex for their subset samples. The scatter here is comparable with the main uncertainties contributed by observational errors in w_{20} and inclination.

7 STAR FORMATION RATE

Ultraviolet (UV) luminosity is an excellent tracer of recent star formation (<100 Myr) but it is affected by dust attennuation. Most UV continuum photons are absorbed by dust and then re-emitted in the mid-infrared (MIR) wavelength. In this study, we use the *Galaxy Evolution Explorer* (*GALEX*; Martin et al. 2005; Morrissey et al. 2007) and *Widefield Infrared Survey Explorer* (*WISE*; Wright et al. 2010) data to estimate the dust un-attenuated and attenuated part of the total SFRs of our galaxies, respectively. It is a known issue that the fluxes obtained from the *GALEX* pipeline are not accurate for extended objects. This is due to the use of small Kron-like elliptical apertures that results in extended sources being broken up into pieces. To circumvent this issue, Seibert et al. (2012) created the GALEX Source Catalog in the Kepler Field (GCAT[7]), in which specific apertures were used to obtain fluxes for the identified extended sources. We obtain the *GALEX* NUV AB magnitudes by matching our galaxies' coordinates to the GCAT via the *GALEX* CasJobs interface. GCAT provides an homogeneous photometry, which includes data from the *GALEX* Medium Imaging Survey (MIS), the All-Sky Imaging Survey (AIS), and the Deep Imaging Survey (DIS) through GR7. We adopt the MIS over AIS magnitudes whenever available. The associated magnitude uncertainty is ~0.15 mag (Seibert et al. 2012).

We follow the same procedure as described in Section 5.2.1 to correct NUV AB magnitudes for the Galactic dust extinction, where $A_{NUV} = 8.2 \times E(B - V)$ (Wyder et al. 2007) is adopted. The intrinsic monochromatic flux $F_{\nu, mono}$ in units of erg s^{-1} cm^{-2} Hz^{-1}
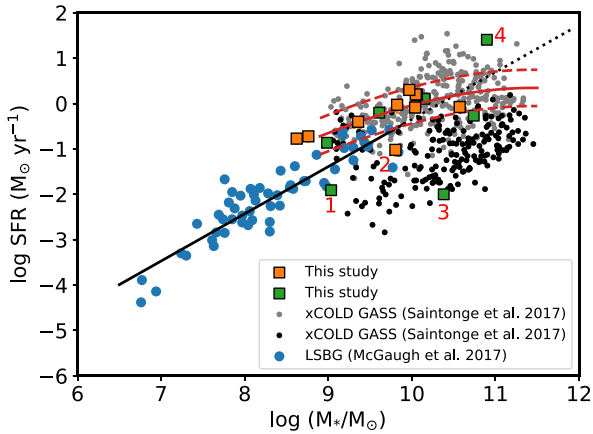
---

[7]https://archive.stsci.edu/prepds/gcat/

Figure 16. Measurements in this study (filled orange and green squares) overlaid on to samples from xCOLD GASS (Saintonge et al. 2017) (black and grey dots) and McGaugh et al. (2017) (blue dots) for the SFR–M_* relations. The solid and dashed black lines represent the fit and extended fit from McGaugh et al. (2017). The red line represent the fit from Saintonge et al. (2016), where the upper and lower boundaries for the ±0.4 dex scatter are represented by red dashed lines.

is calculated with $M_{intrinsic}$ (AB mag) $= -2.5 \log(F_{\nu,mono}) - 48.6$ (Oke 1990). We convert the intrinsic NUV fluxes to luminosities and calculate the NUV SFRs using equation 6 in Schiminovich et al. (2007).

We perform aperture photometry of our galaxies using the *WISE* 22 μm band-4 (*W*4) mosaics produced by Image Co-addition with optional Resolution Enhancement tool (Masci 2013). We calculate the surface brightness radial profile for each galaxy based on the aperture fluxes, and derive the total flux by fitting a two-component Sersic model to the radial profile. The details of the procedure is described in Wang et al. (2017), which follows the method of Jarrett et al. (2012). Subsequently, we calculate the MIR SFR_{W4} using equation (2) of Jarrett et al. (2013). The total SFR $= SFR_{NUV} + SFR_{W4}$, where we assume the dust attenuation is zero if the *W*4 photometry is unavailable and the total SFR will be considered as the lower limit if there is no NUV measurement.

To investigate if our galaxies are actively forming stars, we compare SFRs with the fitted SFR–M_* relations derived from a sample of low surface brightness galaxies (LSBG; McGaugh, Schombert & Lelli 2017) and star-forming galaxies in xCOLD GASS (extended CO Legacy Database for GASS; Saintonge et al. 2017). This relation forms the star formation main sequence (SFMS), where galaxies are undergoing exceptionally high star formation if lie above the SFMS and are quenched if lie below the SFMS. In Fig. 16, we overplot our data (filled orange and green squares), the LSBG data (blue dots) and the xCOLD GASS data (grey and black dots) on to the SFR–M_* plane. The filled orange and green squares represent the total SFR and the lower limit, respectively. Errors in total SFR are relatively small compared with the size of the symbol. The grey and black dots represent the xCOLD GASS galaxies and those without CO(1–0) detections, respectively. The study of McGaugh et al. (2017) covers a stellar mass range of $10^7 - 10^{10}$ M$_\odot$ and extends the SFR down to 10^{-4} M$_\odot$ yr^{-1}. They find a steep slope (solid and black dashed line) for the SFR–M_* relation but a 'flatter' slope if compared to the

relation derived from the Spitzer Infrared Nearby Galaxies Survey sample (not shown), which mostly consists of massive spirals ($M_* \sim 10^{10}$ M$_\odot$) (Kennicutt et al. 2009). The derived SFR–M_* relation (red line) using a large sample of COLD GASS shows a similar flattening (Saintonge et al. 2016). They find that the flattening of SFMS is due to the global decrease of cold gas reservoirs in galaxies rather than the inefficiency in converting cold atomic gas to stars.

We find NGC 5152 and IC 4290 (labelled as 2 and 3, respectively in Fig. 16) fall below the SFMS relation suggesting quenching in star formation. In fact, NGC 5152 is deficient in H I. While LEDA 47428 (labelled as 1) is positioned below the SFMS of both McGaugh and Saintonge's relations, we cannot conclude if it is also quenched in star formation. This is because its SFR is a lower limit, but within the scatter of McGaugh's SFMS relation. NGC 5135 (labelled 4), is a known starburst galaxy, which its SFR is expected to be above the SFMS. Table 6 gives a summary of the photometry and the calculated SFRs of the 34 galaxies.

8 H I KINEMATICS

Analysis of the H I kinematics allows us to probe the dynamical state of galaxies. Tilted-ring fitting has been widely used to derive rotation curves (e.g. de Blok & McGaugh 1997; Oh et al. 2011). The classical fitting procedure based on χ^2-squared minimization is often sensitive to initial estimates of the ring parameters. This makes the fitting subjective, and thus the analysis is usually performed in an interactive manner. Given the large number of resolved galaxies that are expected to be detected in WALLABY, automated softwares such as 2D Bayesian Automated Tilted-ring (2DBAT; Oh et al. 2018b) and 3D Fully Automated TiRiFiC (FAT; Kamphuis et al. 2015) are being developed.

There are 14 galaxies that are resolved by 3–4 beams across their major axes in this study. FAT is not suitable because well-resolved galaxies (e.g. at least five beams across the semimajor axis) are required. While 2DBAT works best for well-resolved and intermediately inclined (20–70°) galaxies, we find that it is still possible to derive rotation curves for some of the galaxies. This section therefore explores the capability of 2DBAT for the future analysis of large samples of WALLABY sources.

To prepare the input for 2DBAT, we first convert the SOFIA source cubelets to the rest systemic velocity frame (V_{sys}). Subsequently, we extract the line-of-sight velocity fields of the galaxies using a single Gaussian fit of XGAUFIT task in GIPSY (Allen, Ekers & Terlouw 1985). Most profile shapes were symmetric, so the Gauss–Hermite option was not applied. We ingest the 0th moment and velocity field maps into 2DBAT. To force 2DBAT to fit low-resolution data, a small ring width of ~ 0.2–0.3 times the beam size was required.

First, 2DBAT determines priors for 2D tilted-ring parameters from an ellipse fit to the input moment maps. It then fits a 2D kinematic model that is constructed using the 2D tilted-ring parameters together with the Einasto halo rotation velocity on the input velocity field. We refer the readers to Oh et al. (2018b) for a detailed description of 2DBAT. The final fits yield four reasonable rotation curves out of the 14 galaxies. In Fig. 17, we show the derived rotation curves for the receding (orange circles) and approaching (red crosses) sides of these galaxies. The 2D tilted-ring fitting for both sides of the galaxies are shown as the blue squares. Given the small number of resolved elements of the galaxies along their major axes (e.g. less than 5), we keep the systemic velocity (V_{sys}), position

Table 6. NUV and MIR photometries of sources and associated star formation rate.

Designation (1)	NUV_{MIS} (AB mag) (2)	NUV_{AIS} (AB mag) (3)	$W4$ (mag) (4)	err_{W4} (mag) (5)	SFR_{NUV} ($M_\odot$ yr^{-1}) (6)	SFR_{W4} ($M_\odot$ yr^{-1}) (7)	SFR ($M_\odot$ yr^{-1}) (8)	err_{SFR} ($M_\odot$ yr^{-1}) (9)
WALLABY J132514−303304	–	–	4.80	0.06	–	1.27	>1.27	–
WALLABY J132533−300521	17.98	–	–	–	0.08	–	0.08	0.02
WALLABY J132541−295013	–	–	1.55	0.06	–	25.37	>25.37	–
WALLABY J132627−301909	18.18	–	–	–	0.07	–	0.07	0.02
WALLABY J132644−300031	17.90	17.90	–	–	0.07	–	0.07	0.02

Note. This table is available in its entirety as Supporting Information with the electronic version of the paper. A portion is shown here for guidance regarding its form and content. Col (1): Designation. Cols (2)–(3): NUV_{MIS}, NUV_{AIS} − *GALEX* NUV AB magnitude obtained from the Medium Imaging Survey and All-sky Imaging Survey. Value has been corrected for the Galactic dust extinction. Cols (4)–(5): *WISE* band-4 22 μm (mid-IR) magnitude and error. Value has been corrected for Galactic dust extinction. Cols (6)–(7): Calculated star formation rates based on the NUV and mid-IR fluxes, respectively. Cols (8)–(9): Total star formation rate $= SFR_{NUV} + SFR_{W4}$ and its error, respectively.
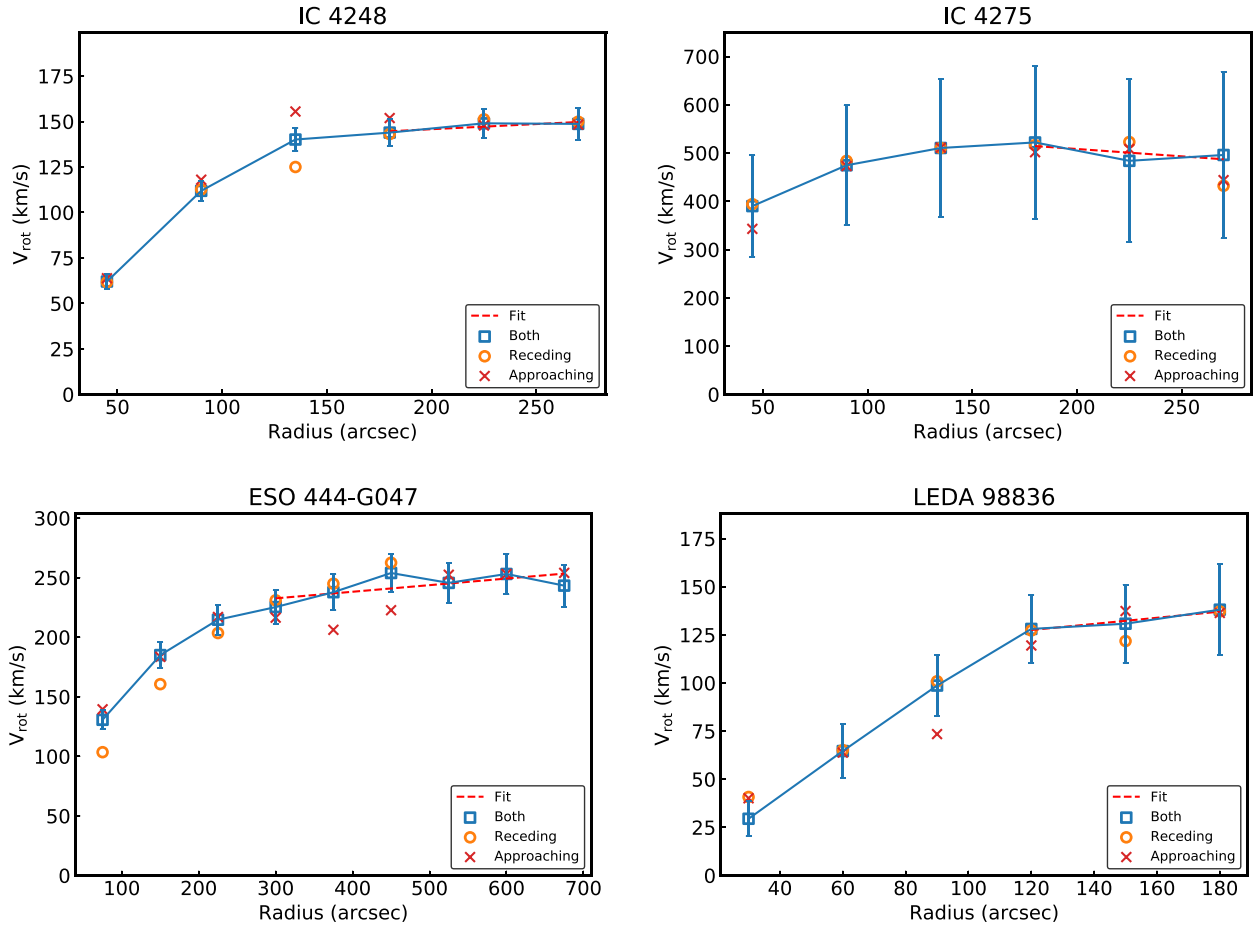*Tidally interacting pair.

Figure 17. Rotation curves derived from 2DBAT. Circles, crosses, and squares represent receding, approaching, and both sides of the rotation curves. The dashed lines show the fit to the 'flat' part of the rotation curves used for estimating the errors.

angle[8] (PA), and inclination (i') constant over the galaxy radii. As such, we cannot investigate any small-scale kinematic structures of our galaxies.

To determine the rotation velocities of these four galaxies, we take the average values of data points that are on the 'flat' part of the rotation curves. We perform a linear least-squares fit to these data

[8]PA is defined as the angle between the major axis of the receding half of the galaxy and north.

points and estimate uncertainties. The red dashed lines in Fig. 17 indicate the data points that are used for fitting and averaging. A summary of the derived parameters is given in Table 7. The V'_{rot} of IC 4275 has a large uncertainty (about ±160 km s^{-1}) due to its low derived inclination, which is different from the optical inclination (∼60°). In Fig. 18, we show the input single Gaussian extracted velocity field maps (left-hand panels), tilted-ring models (middle panels) and residual velocity fields (right-hand panels). These four galaxies exhibit a typical velocity field that is dominated by circular

Table 7. Kinematic parameters.

Galaxy name	V_{sys} (km s^{-1})	i' (°)	PA (°)	V'_{rot} (km s^{-1})	BIC[a]	i[b] (°)	V_{rot}[c] (km s^{-1})
IC 4248	4079	44	286	145 ± 15	4.34×10^3	47	170
IC 4275	4271	12	19	503 ± 160	4.12×10^2	61	136
ESO 444−G047	4356	32	19	246 ± 36	5.66×10^3	66	159
LEDA 98836	4515	16	218	132 ± 71	1.61×10^3	–	–

[a]Bayesian Information Criterion (BIC) is a criterion for model selection among a set of models (Schwarz 1978).
[b]Optical inclination (same as in Table 5).
[c]Rotational velocity (see Section 5.3 and same as in Table 5).
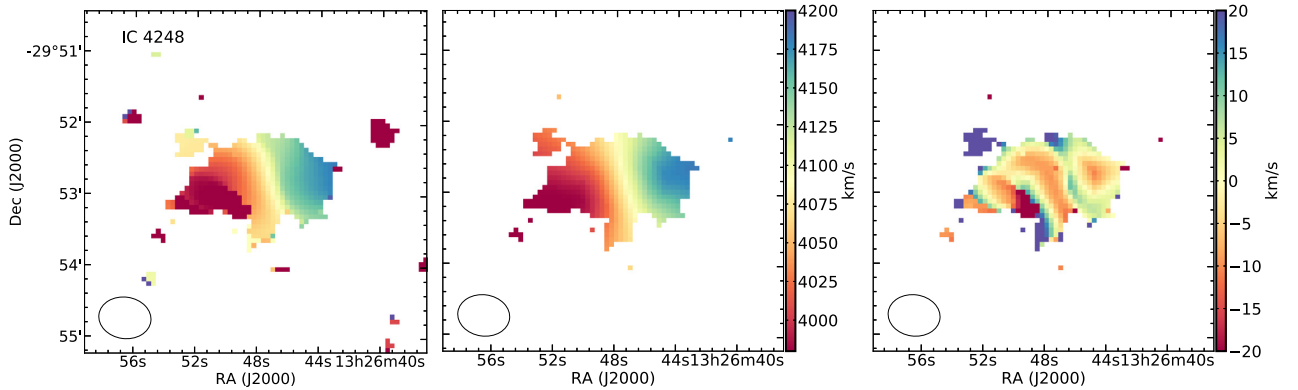
Figure 18. *Left*: Velocity fields extracted using a single Gaussian profile fit. *Middle*: Model velocity fields. *Right*: Residual velocity fields. The synthesized beam of 45 arcsec × 35 arcsec is plotted at the left bottom corner of each sub-plot for reference. Both input observed and model velocity fields have the same colour scale.

motion. The dispersion is within 20 km s^{-1}. The optical morphology and velocity field map of IC 4275 suggests that this galaxy is warped. In contrast, ESO 444−G047 is nearly edge-on with an H I diameter of ∼4 arcmin. Nevertheless, we find that the derived V'_{rot} values from the tilted-ring models of IC 4248, IC 4275, and ESO 444−G047 (see Table 7) are comparable with the V_{rot} calculated from the optical inclination and H I linewidth after taking into account the uncertainties (see Section 5.3 and Table 5). A comparison cannot be made for LEDA 98836 as there is no V_{rot} from the H I linewidth.

9 ENVIRONMENT AND H I MORPHOLOGY

In this section, we refer the reader to the numbering in Fig. 5 and H I morphology shown in Fig. 9. We search for signatures of tidal interaction by examining the H I morphology.

Among the galaxies in LGG 351, we exclude NGC 5135 from the H I morphology discussion due to its incomplete H I profile. We find that the H I morphology at the outer $3 \times N_{H\,I,sen}$ contour of all group members in LGG 351 of G93 catalogue shows evidence of slight distortion. Extended H I gas from the north-east corner of NGC 5182 (#22) is seen towards LEDA 746059 (#24). This feature is unlikely due to noise. NGC 5182 and LEDA 746059 are in close proximity with a projected linear separation of 68.9 kpc, assuming a D_L of 64.6 Mpc.

ESO 444−G047 (#12) is located in the southern outskirts of LGG 351. Its H I is slightly extended at the southern end, pointing towards three nearby H I detected galaxies (i.e. ESO 444−G056, LEDA 98793, and ESO 444−G059: #16, #18, #20, respectively). The lack of detections to the west of ESO 444−G047 is probably

due to the coverage of our observation, where the RMS is higher with only footprint A coverage and the exclusion of beam 31 of footprint B.

There are many H I galaxies around IC 4275 (#28) with LEDA 3082253 (#30) and WALLABY J133201−294119 (#29) being closest to IC 4275. LEDA 3082253 shows an H I extension towards the south-east corner. The optical DECam image also reveals an asymmetry in the stellar distribution, with faint structures extending in the same direction as the H I. Due to their close proximity, tidal interaction is probably the cause of the H I distortion as seen in their extended H I disc. There is no H I debris found. WAL-LABY J133201−294119 is a new galaxy discovered serendipitous through the deep DECam image.

NGC 5152 (spiral) and NGC 5153 (elliptical) are an interacting pair (Arp & Madore 1987). This is particularly interesting as substantial H I debris are often found near massive, early-type galaxies (see e.g. Chung et al. 2009; Saponara et al. 2018). The pair is also part of the subgroup containing NGC 5150. In Fig. 19 (left-hand panel), we show the H I contours from the HIDEEP survey overlaid on to the DSS2r image, where the H I detection is unresolved and identified as HIDEEP J1327−935 (i.e. NGC 5150). With the high spectral and spatial resolution of ASKAP, we are able to resolve it into two H I sources, NGC 5152 (#10) and NGC 5150 (#7) (right-hand panel). There is no H I detection for NGC 5153. A recent molecular gas study of dominant early type galaxies in groups also shows no detection of CO in NGC 5153 (O'Sullivan et al. 2018). This suggests gas depletion in NGC 5153. The extended H I structures of both NGC 5150 and NGC 5152 as well as displacement of H I gas from NGC 5152 provide evidence of tidal interaction between them for the first time. The lack of H I
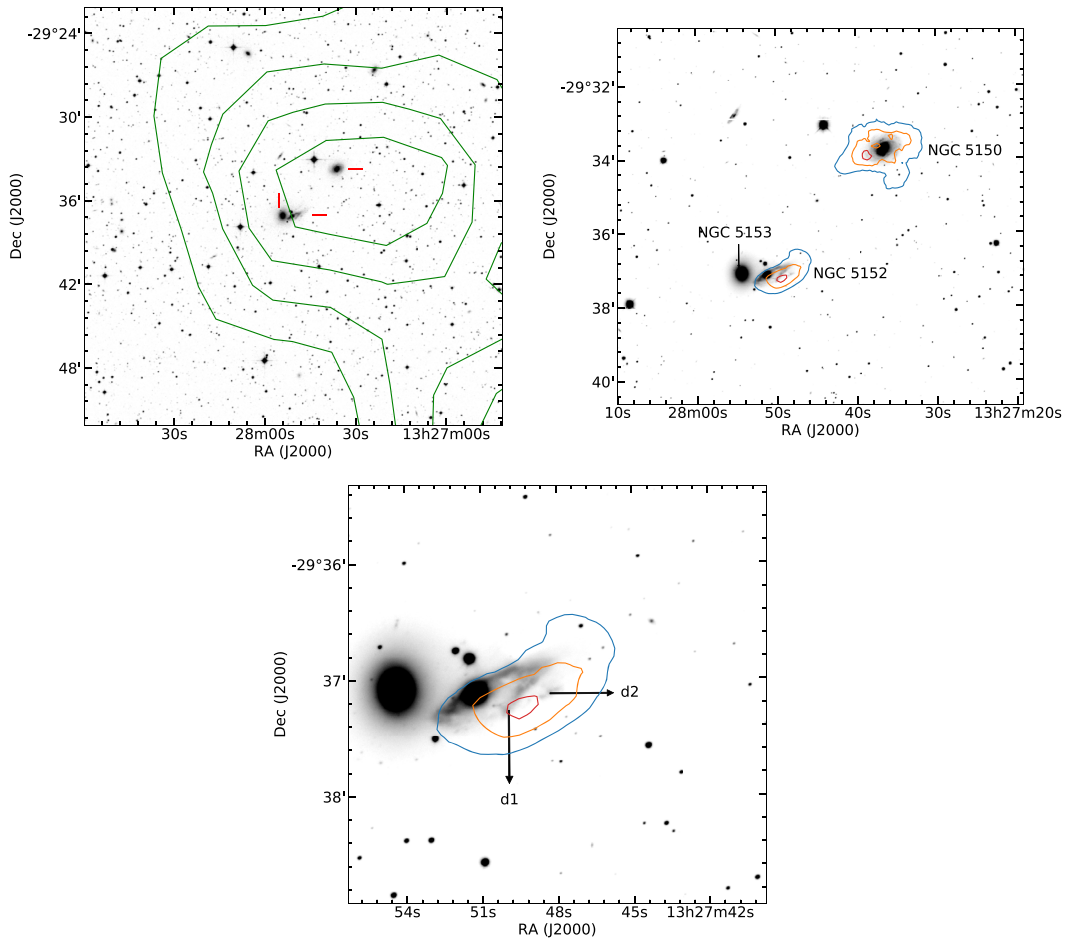
Figure 19. *Top left*: H I intensity contours (green) from the HIDEEP survey ($V_{opt} = 3195-4604$ km s^{-1}) overlaid on to the DSS2r image. The contour levels are 0.05, 0.1, 0.15, and 0.2 Jy beam^{-1}. The positions of NGC 5150, NGC 5152, and NGC 5153 are indicated by the red markers. *Top right*: Zoom in to the NGC 5150 subgroup region with H I column density contours overlaid on to the DECam image (refer the contour levels in Fig. 9). *Bottom*: Zoom in to show the interacting pair, NGC 5152 and NGC 5153, where the tidal dwarf candidates are labelled as d1 and d2 (see Weilbacher et al. 2000).

debris is unexpected, but it is likely that the diffuse H I emission has a lower H I column density ($<10^{20}$ cm^{-2}) that cannot be detected by WALLABY. Another interesting fact for this subgroup is that two tidal dwarf candidates (d1 and d2) have also been reported by Weilbacher et al. (2000) (see bottom panel). The formation of these tidal dwarf galaxies could only be possible via galaxy interactions, when a large amount of gas is expelled and re-collapsed to form such systems.

IC 4248 (#6) is a Sab galaxy. Its optical image shows an interesting ram-pressure/tidally stripped morphology with a few visible 'tentacles'. The H I morphology also shows a distorted structure with a asymmetric morphology similar to the optical morphology. It is known to be interacting with NGC 5135 (#3) (de Vaucouleurs, de Vaucouleurs & Corwin 1976). Unfortunately, we do not find any conclusive evidence of ram-pressure stripping from the tilted-ring fitting given that there is no change in PA. Further investigation is possible with imaging that resolves the inner and outer disc and further down to 10^{19} cm^{-2}.

While we only see hints of tidal interaction within LGG 351 based on H I morphologies, a new interacting pair in the vicinity, WALLABY J133002$-$272832 (#17), is discovered. This pair includes LEDA 47428 and ESO 509$-$G032 (an edge-on galaxy). The DECam image shows a spiral structure at the far side of

ESO 509$-$G032 and a faint extended thin stellar disc towards LEDA 47428. The galaxy pair is located at the northern end of our observed field.

10 FURTHER DISCUSSION

Galaxies in denser cluster environments tend to be deficient in H I as compared to field galaxies (Solanes et al. 2001). Studies of the Fornax (Waugh et al. 2002) and Coma clusters (Bravo-Alfaro et al. 2000) have provided evidence of a decrease of H I with distance from the cluster centre (see also Haynes & Giovanelli 1984). They also show that the optical discs of galaxies near the cluster centre extend beyond their H I discs. This strongly suggests that interactions with the hot IGM (i.e. ram-pressure stripping) is likely the dominant gas removal mechanism in the cluster environment.

Nevertheless, H I deficiency in galaxies is not unique to the cluster environment. It is also found in galaxies of compact and loose groups (see e.g. Verdes-Montenegro et al. 2001; Kilborn et al. 2005). Detection of loose X-ray emission associated with the IGM in Hickson compact groups suggests that tidal interaction rather than ram-pressure stripping is the dominant gas removal mechanism in compact groups (Rasmussen et al. 2008).

As for loose galaxy groups, asymmetries in the outer H I discs of NGC 300 and NGC 55 in the Sculptor group suggest the presence of ram-pressure stripping (Westmeier et al. 2011; Westmeier, Koribalski & Braun 2013). These findings imply that both ram-pressure stripping and tidal interaction play a significant role in removing gas in galaxy groups, but which is the dominant mechanism remains an open question.

There are three galaxies (NGC 5153 and IC 4251 and PGC 47224) in LGG 351 that do not have an H I detection in the observed field. NGC 5152 (in the subgroup of NGC 5150) is considered to be H I deficient and is likely as a result of gas being pulled out to form the tidal dwarfs (see Section 9). Given that IC 4251 and PGC 47224 are located relatively close to the NGC 5150 subgroup and evidence of tidal interaction within the subgroup is seen (see Section 9), we suggest that tidal interaction is likely the main gas removal mechanism for these galaxies despite the lack of H I debris. Further investigation of the hot gas in the region might rule out or support ram-pressure stripping mechanism for these galaxies.

11 SUMMARY AND CONCLUSIONS

WALLABY early science data have allowed us to test and to optimize the analysis techniques and observing strategy for WALLABY. In this process, we have improved continuum subtraction and have found optimal observing window for day time observation to minimize solar interference. We have also tested and demonstrated the performance of ASKAPSOFT, increasing the capability of new versions to deal with early science and full WALLABY data. A statistical analysis of data quality, influence of solar interference and comparison with HIPASS and HIDEEP integrated fluxes is made. The assessment of the effect of solar interference could not be done in previous early science data because there were observed at night. Overall, ASKAP has recovered all the fluxes when compared to single-dish HIDEEP data. Two outliers will need further reassessment with full WALLABY data. We perform source finding using SOFIA and obtain a catalogue of 40 H I sources. Among these sources, two are new H I galaxies that do not have optical identifications and one is a tidally interacting pair. This is the largest WALLABY sample to date. All confirmed H I detections have optical counterparts. We use our measurements to refine LGG 351 group membership, adding 32 new members (including a tidally interacting pair). Further observations are likely to further increase group membership, and resolve membership issues in LGG 351 and the relationship with TSK group 2543. The recession velocity distribution shows that the new galaxy members of LGG 351 are within $\sim$4200–4900 km s^{-1}.

We adopt the 2MASS K_s band to stellar mass relation to derive stellar masses. We also calculate H I masses, H I deficiency parameters, and rotational velocities. The two new H I galaxies are at the low H I mass end of the distribution (log $M_{HI}/M_\odot \sim 8.2$). We find that the galaxies in LGG 351 are generally H I rich. Comparing the atomic gas fraction scaling relation with GASS and xGASS samples indicates that our galaxies follow the general trend of decreasing M_{HI}/M_* as a function of M_*. Our galaxies also follow the BTF relation. We derive the total SFRs of 34 galaxies using NUV and MIR calibration, using archival *GALEX* data in the Kepler field and *WISE* band-4 data. Seventeen galaxies have both total SFR and stellar mass measurements, which allow us to compare with the SFMS determined by McGaugh et al. (2017) and Saintonge et al. (2016). The majority of our galaxies are actively forming stars, with the exception of four galaxies. One of the exceptions is

a confirmed starburst galaxy that lies above the SFMS. The other three lie below the SFMS. The evolutionary state for two out of the three galaxies is inconclusive because it depends on which SFMS relation is considered.

We attempt to perform a tilted-ring fit on our marginally resolved galaxies using 2DBAT. This is the first practical use of 2DBAT on WALLABY data. We successfully derive the rotation curves for four galaxies. Three of the derived V_{rot} values are consistent with the V_{rot} calculated from the H I spectral linewidth and optical inclination. Due to the angular resolution, we cannot study the small-scale kinematic structure. We also present the extracted velocity fields, model, and residual maps for these four galaxies. Investigating the H I morphology of the LGG 351 galaxies, we find evidence of tidal interaction in the NGC 5150 subgroup, NGC 5182, LEDA 3082253 and IC 4248. There is no H I debris found in our studied area. It is likely that any extended diffuse emission has been resolved out by ASKAP with the early science configuration. Full ASKAP-36 WALLABY observations or follow-up targeted H I observations with higher sensitivity would be useful in the search for extended diffuse emission and allow further study the galaxies in greater detail.

This study has shown the excellent performance of SOFIA in searching for sources in ASKAP H I data cubes and the feasibility of using 2DBAT to derive the rotation curves of marginally resolved galaxies. WALLABY early science has also proven to be sensitive enough to detect low-mass dwarf galaxies of the order of 10^8 M$_\odot$ out to a distance of $\sim$60 Mpc. Complementary multiwavelength data are shown to be important in order to study physical processes and their relations with the environment. Our sample is small for some of the derived parameters, such as the star formation and stellar mass, due to the lack of UV, infrared, and optical photometry. The ongoing Skymapper survey, VISTA Hemisphere Survey and extended source catalogue from *WISE* could potentially mitigate the issue of sample size.

REFERENCES

Allen R. J., Ekers R. D., Terlouw J. P., 1985, in di Gesu V., Scarsi L., Crane P., Friedman J. H., Levialdi S., eds, Data Analysis in Astronomy. Plenum Press, New York, p. 271

Arp H., Madore B., 1987, J. Br. Astron. Assoc., 97, 295

Barnes D. G. et al., 2001, MNRAS, 322, 486

Bell E. F., de Jong R. S., 2001, ApJ, 550, 212

Bell E. F., McIntosh D. H., Katz N., Weinberg M. D., 2003, ApJS, 149, 289

Boselli A., Gavazzi G., 2009, A&A, 508, 201

Boselli A. et al., 2010, PASP, 122, 261

Bravo-Alfaro H., Cayatte V., van Gorkom J. H., Balkowski C., 2000, AJ, 119, 580

Brown T. et al., 2017, MNRAS, 466, 1275

Butcher H., Oemler A., Jr, 1978, ApJ, 219, 18

Cardelli J. A., Clayton G. C., Mathis J. S., 1989, ApJ, 345, 245

Catinella B. et al., 2012, MNRAS, 420, 1959 (C12)

Catinella B. et al., 2013, MNRAS, 436, 34

Catinella B. et al., 2018, MNRAS, 476, 875

Chabrier G., 2003, PASP, 115, 763

Chilingarian I. V., Zolotukhin I. Y., 2012, MNRAS, 419, 1727

Chilingarian I. V., Melchior A.-L., Zolotukhin I. Y., 2010, MNRAS, 405, 1409

Chung A., van Gorkom J. H., Kenney J. D. P., Crowl H., Vollmer B., 2009, AJ, 138, 1741

Cohen M., Wheaton W. A., Megeath S. T., 2003, AJ, 126, 1090

Colless M. et al., 2001, MNRAS, 328, 1039

Condon J. J., Cotton W. D., Greisen E. W., Yin Q. F., Perley R. A., Taylor G. B., Broderick J. J., 1998, AJ, 115, 1693

Cortese L., Catinella B., Boissier S., Boselli A., Heinis S., 2011, MNRAS, 415, 1797

Cortese L. et al., 2019, MNRAS, 485, 2656

de Blok W. J. G., McGaugh S. S., 1997, MNRAS, 290, 533

Dekel A., Birnboim Y., 2006, MNRAS, 368, 2

de Vaucouleurs G., de Vaucouleurs A., Corwin J. R., 1976, Second Reference Catalogue of Bright Galaxies, Vol. 1976. University of Texas Press, Austin

Dressler A., 1980, ApJ, 236, 351

Duffy A. R., Meyer M. J., Staveley-Smith L., Bernyk M., Croton D. J., Koribalski B. S., Gerstmann D., Westerlund S., 2012, MNRAS, 426, 3385

Elagali A. et al., 2019, MNRAS, 487, 2797

Fixsen D. J., Cheng E. S., Gales J. M., Mather J. C., Shafer R. A., Wright E. L., 1996, ApJ, 473, 576

For B.-Q., Koribalski B. S., Jarrett T. H., 2012, MNRAS, 425, 1934

For B.-Q., Staveley-Smith L., McClure-Griffiths N. M., 2013, ApJ, 764, 74

For B.-Q., Staveley-Smith L., Matthews D., McClure-Griffiths N. M., 2014, ApJ, 792, 43

Fouque P., Gourgoulhon E., Chamaraux P., Paturel G., 1992, A&AS, 93, 211

Garcia A. M., 1993, A&AS, 100, 47 (G93)

Garcia A. M., Paturel G., Bottinelli L., Gouguenheim L., 1993, A&AS, 98, 7

Giovanelli R. et al., 2005, AJ, 130, 2598

Giovanelli R. et al., 2013, AJ, 146, 15

Grcevich J., Putman M. E., 2009, ApJ, 696, 385

Haynes M. P., Giovanelli R., 1984, AJ, 89, 758

Hibbard J. E., van Gorkom J. H., 1996, AJ, 111, 655

Högbom J. A., 1974, A&AS, 15, 417

Hotan A. W. et al., 2014, Publ. Astron. Soc. Aust., 31, e041

Huchra J. P., Geller M. J., 1982, ApJ, 257, 423

Janowiecki S., Catinella B., Cortese L., Saintonge A., Brown T., Wang J., 2017, MNRAS, 466, 4795

Jarrett T. H. et al., 2012, AJ, 144, 68

Jarrett T. H. et al., 2013, AJ, 145, 6

Johnston S. et al., 2007, Publ. Astron. Soc. Aust., 24, 174

Jones M. G. et al., 2018, A&A, 609, A17

Kamphuis P., Józsa G. I. G., Oh S.-H., Spekkens K., Urbancic N., Serra P., Koribalski B. S., Dettmar R.-J., 2015, MNRAS, 452, 3139

Katz N., Keres D., Dave R., Weinberg D. H., 2003, in Rosenberg J. L., Putman M. E., eds, Astrophysics and Space Science Library, Vol. 281, The IGM/Galaxy Connection. The Distribution of Baryons at z = 0. Kluwer, Dordrecht, p. 185

Kauffmann G., White S. D. M., Heckman T. M., Ménard B., Brinchmann J., Charlot S., Tremonti C., Brinkmann J., 2004, MNRAS, 353, 713

Kennicutt R. C. et al., 2009, ApJ, 703, 1672

Kereš D., Katz N., Weinberg D. H., Davé R., 2005, MNRAS, 363, 2

Kilborn V. A., Koribalski B. S., Forbes D. A., Barnes D. G., Musgrave R. C., 2005, MNRAS, 356, 77

Kleiner D. et al., 2019, MNRAS, 488, 5352

Kollatschny W., Fricke K. J., 1989, A&A, 219, 34 (KF89)

Koribalski B. S., López-Sánchez Á. R., 2009, MNRAS, 400, 1749

Larson R. B., Tinsley B. M., Caldwell C. N., 1980, ApJ, 237, 692

Lee-Waddell K. et al., 2019, MNRAS, 487, 5248 (LW19)

Lewis I. et al., 2002, MNRAS, 334, 673

McConnell D. et al., 2016, Publ. Astron. Soc. Aust., 33, e042

McGaugh S. S., Schombert J. M., Lelli F., 2017, ApJ, 851, 22

McQuinn K. B. W. et al., 2015, ApJ, 812, 158

Madau P., Dickinson M., 2014, ARA&A, 52, 415

Martin D. C. et al., 2005, ApJ, 619, L1

Masci F., 2013, Astrophysics Source Code Library, record ascl:1302.010

Materne J., 1978, in Longair M. S., Einasto J., eds, IAU Symp. Vol. 79, Large Scale Structures in the Universe. D. Reidel Publishing Co., Dordrecht, p. 93

Mauch T., Murphy T., Buttery H. J., Curran J., Hunstead R. W., Piestrzynski B., Robertson J. G., Sadler E. M., 2003, MNRAS, 342, 1117

Meyer M., Robotham A., Obreschkow D., Westmeier T., Duffy A. R., Staveley-Smith L., 2017, Publ. Astron. Soc. Aust., 34, 52 (M17)

Minchin R. F. et al., 2003, MNRAS, 346, 787

Morrissey P. et al., 2007, ApJS, 173, 682

Müller O., Jerjen H., Binggeli B., 2015, A&A, 583, A79

Müller O., Jerjen H., Binggeli B., 2017, A&A, 597, A7

Müller O., Rejkuba M., Jerjen H., 2018, A&A, 615, A96

Oh S.-H., de Blok W. J. G., Brinks E., Walter F., Kennicutt Jr. R. C., 2011, AJ, 141, 193

Oh S. et al., 2018a, ApJS, 237, 14

Oh S.-H., Staveley-Smith L., Spekkens K., Kamphuis P., Koribalski B. S., 2018b, MNRAS, 473, 3256

Oke J. B., 1990, AJ, 99, 1621

Paturel G., Bottinelli L., Fouque P., Gouguenheim L., 1988, ESOC, 435, 28

O'Sullivan E. et al., 2018, A&A, 618, A126

Rasmussen J., Ponman T. J., Verdes-Montenegro L., Yun M. S., Borthakur S., 2008, MNRAS, 388, 1245

Rasmussen J. et al., 2012, ApJ, 747, 31

Reynolds T. N. et al., 2019, MNRAS, 482, 3591 (R19)

Saintonge A. et al., 2016, MNRAS, 462, 1749

Saintonge A. et al., 2017, ApJS, 233, 22

Salpeter E. E., 1955, ApJ, 121, 161

Saponara J., Koribalski B. S., Benaglia P., Fernández López M., 2018, MNRAS, 473, 3358

Schiminovich D. et al., 2007, ApJS, 173, 315

Schlafly E. F., Finkbeiner D. P., 2011, ApJ, 737, 103

Schlegel D. J., Finkbeiner D. P., Davis M., 1998, ApJ, 500, 525

Schwarz G., 1978, Ann. Stat., 6, 461

Seibert M. et al., 2012, American Astronomical Society Meeting Abstracts, #219, p. 340.01

Serra P. et al., 2015, MNRAS, 448, 1922

Skrutskie M. F. et al., 2006, AJ, 131, 1163

Solanes J. M., Giovanelli R., Haynes M. P., 1996, ApJ, 461, 609

Solanes J. M., Manrique A., García-Gómez C., González-Casado G., Giovanelli R., Haynes M. P., 2001, ApJ, 548, 97

Spergel D. N. et al., 2007, ApJS, 170, 377

Springob C. M., Haynes M. P., Giovanelli R., Kent B. R., 2005, ApJS, 160, 149

Tonry J., Schneider D. P., 1988, AJ, 96, 807

Tully R. B., 1980, ApJ, 237, 390

Tully R. B., 2015, AJ, 149, 171

Tully R. B., Shaya E. J., Karachentsev I. D., Courtois H. M., Kocevski D. D., Rizzi L., Peel A., 2008, ApJ, 676, 184

Tully R. B., Rizzi L., Shaya E. J., Courtois H. M., Makarov D. I., Jacobs B. A., 2009, AJ, 138, 323

Tully R. B. et al., 2013, AJ, 146, 86

van de Voort F., Schaye J., Booth C. M., Haas M. R., Dalla Vecchia C., 2011, MNRAS, 414, 2458

Verdes-Montenegro L., Yun M. S., Williams B. A., Huchtmeier W. K., Del Olmo A., Perea J., 2001, A&A, 377, 812

Verdes-Montenegro L., Sulentic J., Lisenfeld U., Leon S., Espada D., Garcia E., Sabater J., Verley S., 2005, A&A, 436, 443

Vollmer B. et al., 2012, A&A, 537, A143

Wang J. et al., 2017, MNRAS, 472, 3029

Waugh M. et al., 2002, MNRAS, 337, 641

Weilbacher P. M., Duc P.-A., Fritze v. Alvensleben U., Martin P., Fricke K. J., 2000, A&A, 358, 819

Wen X.-Q., Wu H., Zhu Y.-N., Lam M. I., Wu C.-J., Wicker J., Zhao Y.-H., 2013, MNRAS, 433, 2946

Wenger M. et al., 2000, A&AS, 143, 9

Westmeier T., Braun R., Koribalski B. S., 2011, MNRAS, 410, 2217

Westmeier T., Koribalski B. S., Braun R., 2013, MNRAS, 434, 3511

Westmeier T., Staveley-Smith L., Calabretta M., Jurek R., Koribalski B. S., Meyer M., Popping A., Wong O. I., 2015, MNRAS, 453, 338

Wong O. I. et al., 2006, MNRAS, 371, 1855

Wright E. L. et al., 2010, AJ, 140, 1868

Wyder T. K. et al., 2007, ApJS, 173, 293

Yang X., Mo H. J., van den Bosch F. C., Pasquali A., Li C., Barden M., 2007, ApJ, 671, 153

York D. G. et al., 2000, AJ, 120, 1579

SUPPORTING INFORMATION

Supplementary data are available at *MNRAS* online.

Figure 6. Spectrum of individual sources obtain from SOFIA.

Figure 9. Integrated H I column density maps of individual sources overlaid on to DSS2r or DECam images.

Figure 10. Velocity field maps of individual sources.

Figure 18. Input velocity field maps, tilted ring models, and residual velocity fields.

Table 4. Source catalogue and derived parameters.

Table 5. Photometry of sources and relevant derived parameters.

Table 6. NUV and MIR photometries of sources and associated star formation rate.

Please note: Oxford University Press is not responsible for the content or functionality of any supporting materials supplied by the authors. Any queries (other than missing material) should be directed to the corresponding author for the article.

This paper has been typeset from a TEX/LATEX file prepared by the author.